31th EUROPEAN ROTORCRAFT FORUM

Florence, Italy - September 13-15, 2005

Paper 45

Analysis Methodology for 3C PIV Data

Berend G. van der Wall, DLR Braunschweig, Germany
Hugues Richard, DLR Göttingen, Germany

In the past, significant effort was placed in flow field measurements of rotor wake vortices. This was driven by the importance of the rotor blade tip vortices for the blade-vortex interaction noise radiation of helicopters. The goal is to obtain reliable data for the generation of a generalized model of tip vortices, including their generation and roll-up, and their aging while passing through the rotor disk and interacting with some of the revolving blades. In 2001 DLR, ONERA, NASA Langley, US Army AFDD and DNW performed the HART II test in the large low-speed facility of the DNW with a 40% Mach scaled model rotor of the Bo105. Major emphasis was placed on three component particle image velocimetry (3C-PIV) measurements of the blade tip vortices. They were traced from their creation in the second and third quadrant of the rotor disk to the rear of the rotor, including blade-vortex interaction (BVI). This paper deals with difficulties associated with the analysis of such 3C-PIV measurements and with the methodologies that need to be applied to overcome these difficulties.

Nomenclature

Abbreviations

AV	Average value
BL	Baseline case
BVI	Blade Vortex Interaction
HART	HHC Aeroacoustic Rotor Test
HHC	Higher Harmonic Control
LDV	Laser Doppler Velocimetry
PIV	Particle Image Velocimetry
2C, 3C	Two, three Component

Symbols

a_∞	speed of sound, m/s
c	chord, m
C_T	thrust coefficient, $= T/(\rho\pi\Omega^2 R^4)$
L_m	measurement volume length, m
M_H	hover tip Mach number, $= \Omega R/a_\infty$
N_b	number of blades
n	Vatistas swirl shape parameter
r	radial coordinate, m
r_c	core radius, m
R	rotor radius, m
t	time, s
T	thrust, N
u, v, w	velocity components, m/s
V	velocity, m/s
x, y, z	coordinates, m
α	angle of attack, deg
β	vortex inclination angle, deg
Γ	circulation, m^2/s
λ_2, Q	flow field operators, $(rad/s)^2$
μ	advance ratio, $= V/(\Omega R)$
ν	kinematic viscosity, m^2/s
ρ	air density, kg/m^3
σ	solidity, $= N_b c/(\pi R)$
σ	standard deviation
ψ	azimuth, $= \Omega t$, deg
ω	vorticity, rad/s
Ω	rotor rotational frequency, rad/s

Indices

b	blade
S	shaft
s	swirl
v	vortex

1 Introduction

Flow measurement techniques of today are non-intrusive using either the Doppler effect in Laser Doppler Velocimetry (LDV) or the shift of particle images in two successive exposures with very small time interval between them (Particle Image Velocimetry, PIV). LDV typically has a very small probe volume, and for field measurements the volume must scan the area to be observed. PIV provides a large area with the instantaneous velocity field.

Often the flow structures to be observed are subject to random variations, either caused by model motion, natural air turbulence, or flow field instabilities. As an example, dynamic stall measurements are repeating the phenomenon cycle by cycle in general, but each cycle has strong indi-

Reference	R/m	c/mm	M_H	μ	C_T/σ	L_m/r_c	pixel/k^2	$\Delta t/\mu s$	$\Delta\psi/^o$	N_I
Heineck [1]	2.27	190.5	0.615	0.0	0.094	2.60	1 x 1	40	0.2	500
Martin [2]	0.41	44.0	0.265	0.0	0.087	1.31	1 x 1	50	0.6	20
Raffel [4]	0.50	50.0	0.231	0.2	0.063	1.38	3.6 x 2.4	12	0.1	100
TRAM [3]	1.45	140.0	0.630	0.15	0.085	1.83	1 x 1	20	0.17	100
ERATO [5]	2.10	70.0	0.617	0.17	0.063	1.93	1.28 x 1	50	0.3	50
Richard [6]	4.92	270.0	0.617	0.0	0.064	0.47	1.28 x 1	10	.025	1
Kato [7]	1.00	65.0	0.308	0.16	0.097	0.50	1.28 x 1	6	.036	900
ATIC-1 [8]	2.00	110.7	0.618	0.16	0.073	1.19	1.28 x 1	50	0.3	50
ATIC-2 [9]	2.00	110.7	0.618	0.16	0.073	1.86	1.28 x 1	50	0.3	30
McAlister [10]	0.96	103.9	0.260	0.0	0.095	0.65	2 x 2	5	.026	25
HART II[1] [12]	2.00	121.0	0.634	0.15	0.057	1.96	1.28 x 1	17	0.1	100
HART II[2] [12]	2.00	121.0	0.634	0.15	0.057	0.51	1.28 x 1	17	0.1	100

Table 1: Comparison of PIV measurement resolution, $r_c = 0.05c$. [1] large and [2] small observation area, N_I = number of images per position.

vidual time history in the post-stall regime. In helicopter rotor wakes, the model is subject to small motions that are non-harmonic in terms of rotor frequency, and thus blade tip vortex creation locations and the local blade aerodynamics are slightly different in each revolution. Since PIV provides an instantaneous measurement of the complete area, this technique is thought of as superior to LDV. A stereo arrangement allows to resolve for the third flow component (3C).

1.1 Rotor blade tip vortex measurements using PIV

In Tab. 1 various rotor tests with application of PIV are listed with their operational conditions. Small scale rotors are often operated at half or a third of the tip Mach number [2, 4, 7] of full scale rotors [6] or large-scale models [1, 3, 5, 8, 9, 12].

The 3C-PIV technique was applied to a lightly loaded, 2-bladed, untwisted hovering rotor in [1], where the necessity of conditional averaging was emphasized. A comparison of 3C-LDV and 3C-PIV on a 1-bladed small-scale model rotor was given in [2]. Therein the importance of the length of the measurement volume L_m, related to the core radius r_c to be measured, is shown. In case of PIV or other camera based techniques, the advantage of the instantaneous measurement of an entire area is associated with a smaller spatial resolution, which is defined by the size of the cross-correlation windows. The conclusion was made that the results of (ensemble averaged) PIV data are not at all sufficient to resolve tip vortex core properties. Several PIV application to rotor blade tip vortices are listed in Tab. 1 with the operational data and the resolutions obtained with PIV. In 1998 PIV was applied to a small scale tilt rotor model (TRAM) in DNW operated in descending forward flight [3]. Vortices at an age of about one revolution right before interacting with a blade were investigated and core radii of about $r_c = 0.25c$ were measured.

A 2C-PIV measurement was also compared to 3C-LDV measurements in [4], where blade tip vortices of a 4-bladed rectangular small scale model rotor were measured in forward flight. These data indicate the superiority of PIV compared to LDV due to both sufficient spatial resolution as well as the completeness of the instantaneous area measurement with all turbulent structures included. A 2C-PIV test on a large scale model rotor with swept back tapered blade tips was performed during the ERATO program [5]. For the vortices found, six vectors were within the core diameter, which is not enough to analyse the vortex properties. It was concluded that for good vortex core measurements the resolution had to be increased by a factor of about four. With a higher resolution following this result a 2C-PIV measurement was performed at a full-scale Bo105 helicopter while standing on ground but generating a thrust of 2000kg to match the thrust condition planned for the HART II test [6]. Vortex core radii of $r_c = 0.045c$ and peak swirl velocities of $V_{s,max} = 0.42\Omega R$ were measured which corresponds well with the model rotor hover measurements using LDV, for example [2].

3C-PIV measurements of tip vortices on a model rotor in forward flight was performed successfully in the NAL wind tunnel with comparable resolution [7]. The mesurement plane was parallel to the wind tunnel flow such that the vortex axis was inclined significantly at an angle of approximately 50^o to it and the results needed a correction accounting for this. Vortices were traced downstream at $y = 0.76R$ and core radii of $r_c = 0.04c$ with peak swirl velocities of $V_{s,max} = 0.15\Omega R$ were found. Another test called ATIC was performed twice at DNW using 2C-

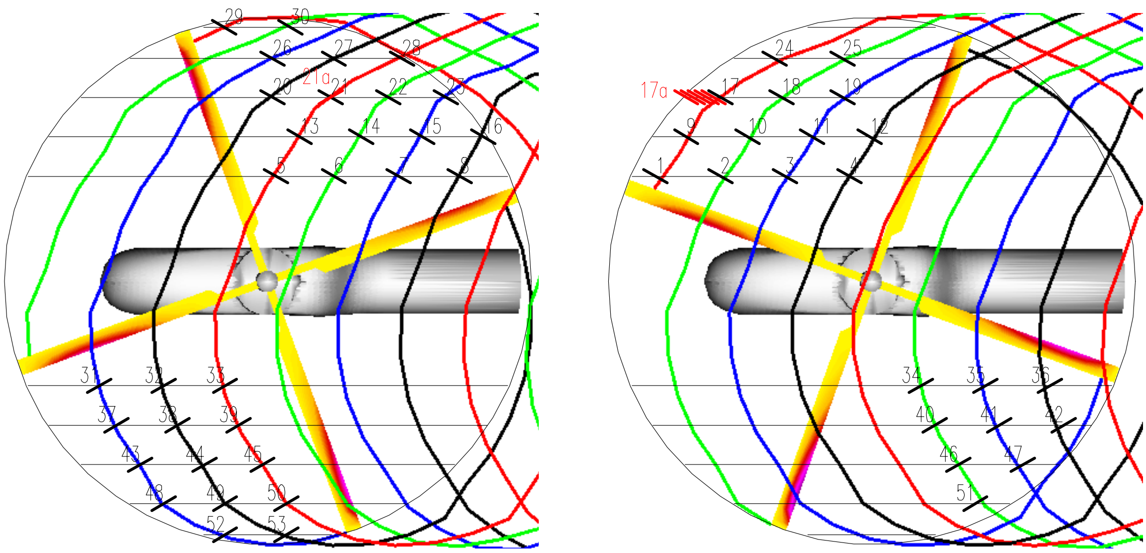

(a) $\psi = 20^o$

(b) $\psi = 70^o$

Figure 1: PIV measurement locations in the rotor disk for the BL case.

PIV in 1998 [8] and 2000 [9], using 5-bladed sets of a Bo105 model rotor and an advanced design. In both tests, the vortex was traced downstream at $y = 0.67R$ at a view angle upstream selected in a way to cut the vortex axis orthogonal. Several advance ratios were investigated, including HHC conditions. Young vortices were measured with core radii of $r_c = 0.05c$ and less, with peak swirl velocities of $V_{s,max} = 0.04 - 0.08\Omega R$.

A recent application to a two-bladed medium scale model model rotor at low tip Mach numbers in low vertical climb was presented in [10]. Core radii of $r_c = 0.05c$ and maximum swirl velocities of up to $V_{s,max} = 0.44\Omega R$ were found, and a void in the vortex center that hindered an analysis of the flow field therein. Vortices were found to be elliptical to some extent.

1.2 PIV application in HART II

In 2001, the Higher Harmonic Control Aeroacoustic Rotor Test II (HART II), commonly performed by DLR, ONERA, NASA Langley, US Army AFDD in the large low-speed facility of the DNW [11, 12] was extensively using 3C-PIV for rotor wake measurements. The rotor is a 40% Mach scaled and dynamically scaled model of the B0105 main rotor with four blades, rectangular planform, $-8^o/R$ linear twist, a radius of 2m, chord of 0.121m and a solidity of $\sigma = 0.077$. The operational condition was at an advance ratio of $\mu = 0.151$, tip Mach number of 0.641, a thrust coefficient of $C_T = 0.0044$ representing a lightly loaded rotor ($C_T/\sigma = 0.0571$, this is representative for a 2ton Bo105 helicopter). Measurements were performed in a 6^o descending flight condition with strongest BVI noise radiation throughout the rotor disk. Also, higher harmonic control (HHC) at 3/rev was applied with a blade root pitch amplitude of 0.8^o and a phase of 300^o for minimum noise radiation and 180^o for minimum vibration. The conditions are described in detail in [12].

One important parameter to characterize the quality of a measurement with respect to vortex core analysis is the ratio of the measurement length with respect to the core radius (L_m/r_c), which will be addressed in Sect. 2.1. Another important parameter is the time delay between two successive images. If chosen too small the particles will move within subpixel range. Too large time delays allow too much particles to leave the second image and new ones to enter it which might be responsible for spurious vectors. However, this must be adopted to the maximum flow velocities to be measured and also to the recording conditions, as there are particle density, laser intensity and background light. In Tab. 1 the measurement resolution L_m/r_c, the time delay Δt and the associated range of blade motion $\Delta\psi$ during the measurement is given for various tests. The HART II measurements are among the smallest values in both time delay and relative blade motion, and also for the spatial resolution, based on 5% chord.

In HART II, more than 300 measurements of blade tip vortices and vortices created inboard of the tip were made. The test set-up, measurement techniques applied, and some representative results were reported in detail in [12]. Details about PIV data acquisition and PIV processing from raw data images to vector maps were presented in [13]. General information about PIV and vector field analysis can be found in [14].

Major emphasis was placed on 3C-PIV measurements of rotor blade tip vortices in conditions with strong BVI, i.e. at a typical descent angle of 6^o at an advance ratio of $\mu = 0.151$. Two 3C-PIV systems were applied simultaneously. DNW operated a system with windows of 0.46m by 0.37m size while the DLR system had different lenses, resulting in a window size of 0.15m by 0.13m. The large observation window was intended for an overview of the area while the small window was intended for vortex analysis, i.e. the identification of vortex parameters like core radius, maximum swirl velocity, swirl velocity profile, axial flow, circulation etc..

While the HHC conditions showed locally negative loading at the blade tips at some range of azimuth this was not the case for the BL condition. At any location with negative loading at the blade tip area the tip vortex has opposite sense of rotation. Inboard, the loading turns to lift and distributed vorticity is shed into the wake along the span, which later on rolls up into a vortex. In these cases pairs of counter-rotating vortices were present in the flow and both of these were measured by PIV systems.

About 330 measurements were made at 70 locations distributed in the rotor disk, see Fig. 1 for 52 of them. The remaining locations were devoted to measurement of multiple vortex systems which occurred in HHC cases. The measurement plane is vertical and rotated by $\pm 30^o$ in order to have the majority of vortices almost orthogonal to the measurement plane, at least from the top view. Each of these measurements were made with both PIV systems and with 100 repeats such that about 66000 vector maps are available for analysis. Since this cannot be performed by hand, automated procedures had to be developed. Several topics have to be addressed for the analysis:

- window size and overlap, Sect. 2.1
- spurious vectors, Sect. 2.2
- field operators and gradients, Sect. 2.3, 2.4
- vortex center detection, Sect. 2.5
- model and camera support movement, vortex wander, Sect. 2.6
- time averaging, Sect. 2.6
- mean velocities, Sect. 2.7
- rotation, Sect. 2.8
- disturbing structures, Sect. 2.9
- parameter identification, Sect. 2.10

Some analysis has been made in the past with identification of some of the parameters [15, 16]. The importance of rotation into the vortex axis system was shown in [17].

In the following sections an analysis methodology is presented that addresses each of these topics. Next, in Sect. 3 this is tested using numerically generated virtual 3C-PIV data to verify the analysed results. Thereafter, the methodology is applied to exemplary HART II data in Sect. 4.

2 Analysis methodology

In all figures of this paper with the in-plane velocity vectors, only every 5th vector is shown in both directions for the sake of visibility.

2.1 Cross-correlation: overlap and window size

The vector fields described in the following were obtained by cross-correlation analysis of interrogation windows with different sizes as presented in [13]. The main parameter which defines the spatial resolution of the measurements beside the interrogation window size is the overlap of the windows. Both parameters affect the result obtained and thus the information which can extracted like the vortex radii and the maximum swirl velocity.

Fig. 2 shows the extracted core radius as well as the maximum velocity as a function of the window overlap obtained by a windows averaging technique which simulates the effect at a flow field given by a Vatistas model [18]. For the model a core radius of $r_c = 0.0435c$ and a swirl velocity of $V_{s,max} = 0.0312\Omega R$ was used. The parameter used allowed to model a young vortex quite similar to the ones measured during the HART II campaign of the advancing side of a rotor in forward flight with respect to the peak-to-peak velocity and core radius. Different window sizes from $0.3878 \le L_m/r_c \le 3.1027$ have been simulated and analyzed. 16x16, 20x20, 24x24 and 32x32 pixel window sizes correspond to the window sizes used during the HART II processing for the small field of view (DLR: $L_m/r_c = 0.3878, 0.4867, 0.5856, 0.7757$), while the window sizes of 64x64 and 128x128 pixel are additionally given (they correspond to $L_m/r_c = 1.5513$ and 3.1027). Also, the 32x32 pixel window size for the large field of view of DNW data, corresponding to $L_m/r_c = 2.2548$ is included. It can easily be seen in Fig. 2, that all the curves are converging to different values. The first (and expected) consequence of the simulation is, that only small interrogation windows ($L_m/r_c < 0.78$) approach the values of the model ($r_{c,exp}/r_c = 1$ and $V_{s,max,exp}/V_{s,max} = 1$) to a sufficient degree with errors less than 5% for this case.

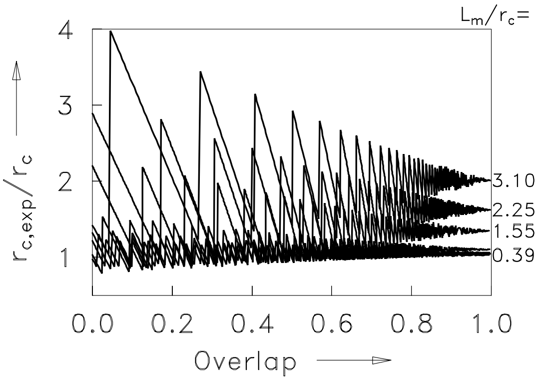

(a) Effect on core radius

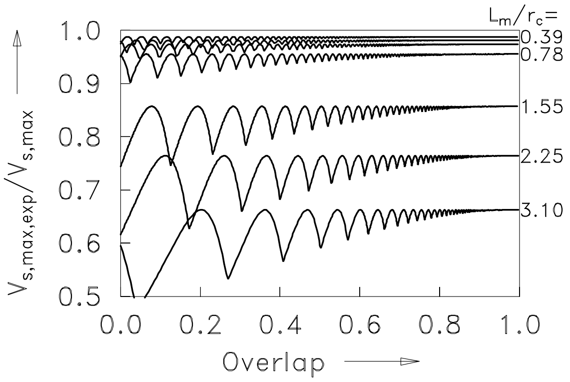

(b) Effect on maximum swirl

Figure 2: Effect of correlation window overlap on accuracy of core radius and swirl velocity for different window sizes.

The second, relatively severe effect that can be observed is the oscillation of the curves, resulting in a random effect. Maximum velocities will be obtained when the center point of an interrogation window falls onto the maximum in the velocity profile. This clearly indicates, that a massive oversampling can be used in order to reduce the scatter of the extracted parameters even if the bias caused by the limitations of larger interrogation windows can not be avoided. The latter can only be obtained by a higher resolution during the test, for example by an increased optical resolution. Since the evaluation of the HART II data base the PIV algorithms have continously been improved. Especially the window deformation technique described by [19] seems to be best suited for the evaluation prior to the vortex parameter extraction. However, new algorithms developed at DLR, which have proven excellent performance during a world wide challenge [20], did not show significant improvement with respect to the HART II evaluation.

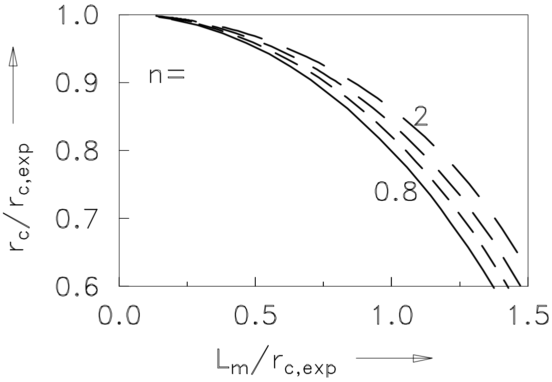

(a) Effect on core radius

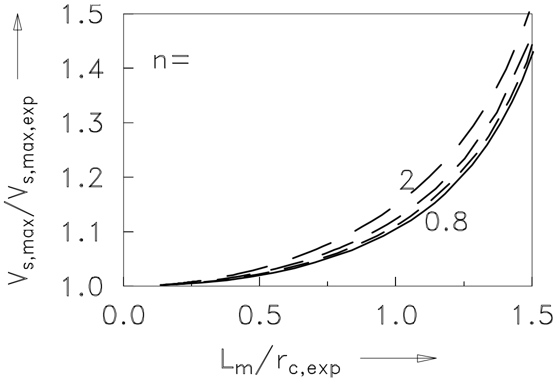

(b) Effect on maximum swirl

Figure 3: Effect of correlation window size on accuracy of core radius and swirl velocity. Solid: $n = 0.8$, increasing dash length: $n = 1, 1.3, 2$.

Based on the same simulation method, the following graphs can be plotted in order to estimate the effect of the window size on the core radius and the maximum velocity at the core radius, see Fig. 3. They both depend on the coefficient n, which has been used in the Vatistas model.

A comparison of the ratio L_m/r_c using the assumption of a core radius of $r_c = 0.05c$ for equivalence of comparison is given in Tab. 1. As pointed out in [2] the ratio L_m/r_c should be less than 0.2 for flows without streamline curvature, and even less when such curvature is present, like near the vortex core. From Tab. 1 it can be seen that the PIV system used in HART II performs well compared to the others, and can even be improved by using 16x16 pixel cross-correlation windows instead of the 24x24 size used in this paper, which would result in $L_m = 0.33r_c$. Modern cameras with double resolution would result in half of the value, and very dense seeding allows for further reduction of the size of the cross-correlation windows. Thus, the requirements of $L_m < 0.2r_c$ for PIV systems are well at hand today.

2.2 Spurious vector elimination

Spurious vectors often result when surfaces are reflecting the laser light. They create a background pattern in the images that does move differently compared to the scattered particle movement in the images. As long as the reflections are of low intensity a high pass filtering can alleviate this, but often the reflections are so strong that the camera pixels are completley saturated and no particles of the flow seeding can be identified. Spurious vectors also are a result of low seeding density when too few particles are within the cross-correlation windows, or due to a too large time delay. They must be eliminated before an analysis of the vector field can start.

As long as these vectors are not clustered they can be identified by statistical methods, comparing the vector of interest with its surroundings (usually ± 1 or 2 indices in both directions) in terms of the mean value and the standard deviation. Thresholds for allowed ranges in both parameters have to be established. Vectors identified to be spurious then are replaced by the mean value of their surroundings. Only a small amount of spurious vectors was observed in the HART II data and most of them were removed using this method. Due to the great number of recordings with different flow conditions the thresholds used were always slightly overestimated in order to ensure that no good vectors are removed. As a consequence, most of the outliers were removed, but probably not all.

An example is shown in Fig. 4 for the effect of 5% of spurious vectors (425 of 8500) on the vorticity before and after their removal. The data are numerically generated using a Vatistas vortex [18], adding 5% of maximum swirl as random noise. 95% of these vectors were identified and replaced by the mean value of the neighboring vectors, they are marked as red arrows. The spurious vectors also affect the computation of the vortex center location which can be seen in Fig. 5 with the swirl velocity profile. Here the thickness of the band with the majority of data indicates that the vortex center was not properly identified, and the large scatter around is due to the spurious vectors. After identification and removal of the spurious vectors the vorticity distribution clearly shows the vortex, plus the data noise which is not affected by the algorithm. The swirl velocity profile also is very clean now and the small thickness of the band of data indicates that the vortex center is correctly identified now.

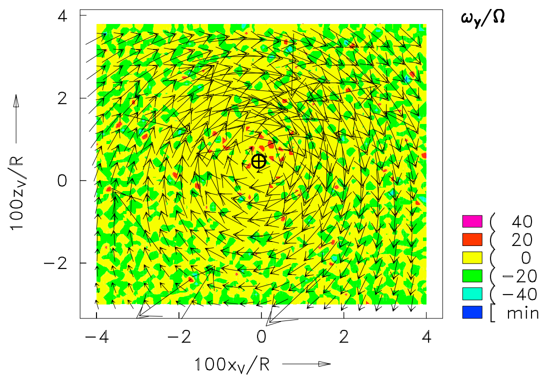

(a) raw data

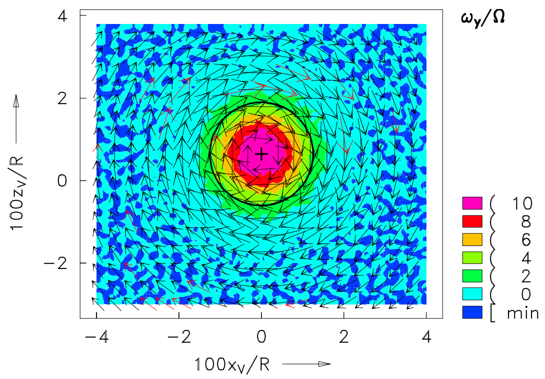

(b) 404 spurious vectors removed

Figure 4: Effect of spurious vectors on vorticity.

2.3 Operators indicating a vortex

For identification of a vortex center flow field operators are used that have large values in the vortex core, where large gradients in the flow components are present. The most common operators are the vorticity ω_y, and the Eigenvalues of the velocity gradient tensor λ_2, and the discriminant of the characteristic equation Q [21, 22].

Typical vortical features of spiral and closed stream lines are observed at special singular points, i.e., the spiral and center points, where often, but not necessarily, a pressure minimum is found as well. In a mathematical way these points are described by complex Eigenvalues of the velocity gradient tensor $\mathbf{A} = \mathbf{S} + \mathbf{\Omega}$ which is composed of a strain tensor $\mathbf{S}$ and the vorticity tensor $\mathbf{\Omega}$ [23]. This leads to the discriminant operator Q derived hereafter. Another definition proposed starts from the gradient operator applied to the Navier-Stokes equation and leads to the Eigenvalues of the tensor $\mathbf{S}^2 + \mathbf{\Omega}^2$, which must be negative [21].

Based on the 2D measurement plane with $x - z$ coordinates and the in-plane velocities u and w,

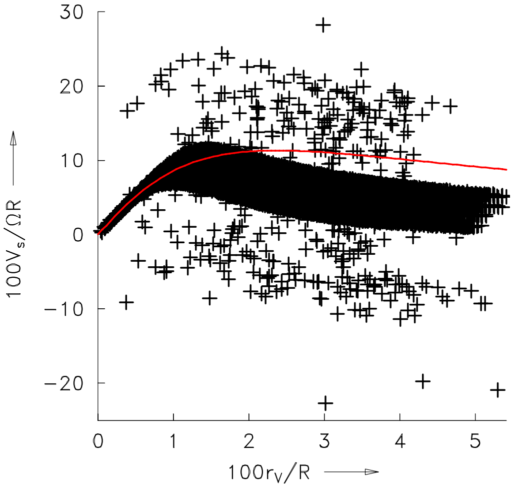

(a) raw data

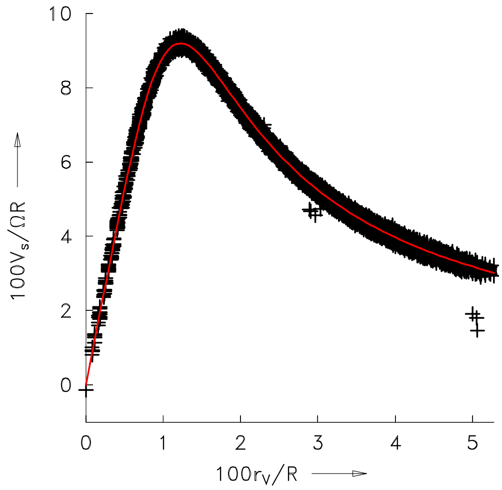

(b) spurious vectors removed

Figure 5: Effect of spurious vectors on swirl velocity. Red line: best fit of Vatistas vortex model.

the velocity gradient tensor is grad$\vec{V} = d\vec{V}/d\vec{r} = \mathbf{A}$.

$$
\begin{aligned}
\frac{d\vec{V}}{d\vec{r}} &= \begin{bmatrix} \frac{\partial u}{\partial x} & \frac{\partial w}{\partial x} \\ \frac{\partial u}{\partial z} & \frac{\partial w}{\partial z} \end{bmatrix} \\
&= \begin{bmatrix} \frac{\partial u}{\partial x} & \left(\frac{\partial w}{\partial x} + \frac{\partial u}{\partial z}\right)/2 \\ \left(\frac{\partial u}{\partial z} + \frac{\partial w}{\partial x}\right)/2 & \frac{\partial w}{\partial z} \end{bmatrix} \\
&+ \begin{bmatrix} 0 & \left(\frac{\partial w}{\partial x} - \frac{\partial u}{\partial z}\right)/2 \\ \left(\frac{\partial u}{\partial z} - \frac{\partial w}{\partial x}\right)/2 & 0 \end{bmatrix} \\
&= \begin{bmatrix} \epsilon_{xx} & \epsilon_{xz}/2 \\ \epsilon_{zx}/2 & \epsilon_{zz} \end{bmatrix} + \begin{bmatrix} 0 & -\omega_y \\ \omega_y & 0 \end{bmatrix} \\
&= \mathbf{S} + \mathbf{\Omega} \;=\; \mathbf{A}
\end{aligned}
$$

The first matrix represents the strain tensor $\mathbf{S}$ with elongational strain in the diagonal and the shear strains in the off-diagonal elements. Vorticity is in the second antisymmetric matrix $\mathbf{\Omega}$. Determinant and trace are defined as

$$
\begin{aligned}
\det \mathbf{A} &= \frac{\partial u}{\partial x}\frac{\partial w}{\partial z} - \frac{\partial u}{\partial z}\frac{\partial w}{\partial x} \\
\mathrm{tr}\mathbf{A} &= \frac{\partial u}{\partial x} + \frac{\partial w}{\partial z}
\end{aligned}
$$

A vortex is characterised by the invariance of the velocity gradient tensor $\mathbf{A}$. This requires that the determinant is greater zero and the Eigenvalue λ of the characteristic equation to be complex, i.e. the discriminant Q must be below zero.

$$
\begin{aligned}
0 &= \lambda^2 - \lambda\,\mathrm{tr}\mathbf{A} + \det\mathbf{A} \\
\lambda_{1,2} &= \mathrm{tr}\,\mathbf{A}/2 \pm \sqrt{Q} \\
Q &= (\mathrm{tr}\,\mathbf{A})^2/4 - \det\mathbf{A} < 0
\end{aligned}
$$

Following the definition that the second and third Eigenvalue of $\mathbf{S}^2 + \mathbf{\Omega}^2$ must be below zero, it follows that either

$$
\begin{aligned}
\lambda_2 &= \left(\frac{\partial u}{\partial x}\right)^2 + \frac{\partial u}{\partial z}\frac{\partial w}{\partial x} < 0 \qquad \textit{or} \\
\lambda_2 &= \left(\frac{\partial w}{\partial z}\right)^2 + \frac{\partial u}{\partial z}\frac{\partial w}{\partial x} < 0
\end{aligned}
$$

The mean value of both is used for this paper. The vorticity ω_y, the discriminant Q and the Eigenvalue λ_2 of the tensor $\mathbf{S}^2 + \mathbf{\Omega}^2$ are thus defined by

$$
\begin{aligned}
\omega_y &= \left(\frac{\partial u}{\partial z} - \frac{\partial w}{\partial x}\right)/2 \\
Q &= \frac{\left(\frac{\partial u}{\partial x} + \frac{\partial w}{\partial z}\right)^2}{4} + \frac{\partial w}{\partial x}\frac{\partial u}{\partial z} - \frac{\partial u}{\partial x}\frac{\partial w}{\partial z} \\
\lambda_2 &= \frac{\left(\frac{\partial u}{\partial x}\right)^2 + \left(\frac{\partial w}{\partial z}\right)^2}{2} + \frac{\partial w}{\partial x}\frac{\partial u}{\partial z}
\end{aligned}
$$

2.4 Velocity gradients

The flow field derivatives (or velocity gradients) are a pre-requisite needed for the computation of the criteria of a vortex. A first suggestion is to apply the center difference approach, which is one-dimensional. For the 50% overlap used in HART II data, the vectors separated by 2 in their indices are independent from each other.

$$
\left.\frac{\partial u}{\partial x}\right|_{i,j} = \frac{u_{i+1,j} - u_{i-1,j}}{x_{i+1,j} - x_{i-1,j}}
$$

In a sheared grid the derivative at i, j requires velocity components along the x coordinate direction. Then, they have to be interpolated from the grid which complicates the procedure.

However, as pointed out in [14], the data are 2-dimensional and thus the local gradient in any direction should also depend on the surrounding flow. Based on the line integral for the circulation of the area around the point of interest in discretized form the flow gradients at i, j can be expressed in terms of surrounding flow components, i.e. by the center differences at $j-1$, j and $j+1$. For equidistant grid spacing,

$$\left.\frac{\partial u}{\partial x}\right|_{i,j} = \frac{\left.\frac{\partial u}{\partial x}\right|_{i,j-1} + 2\left.\frac{\partial u}{\partial x}\right|_{i,j} + \left.\frac{\partial u}{\partial x}\right|_{i,j+1}}{4}$$

The derivative in the other direction is obtained by exchanging the x to z, i to j and j to i. In general, the center difference approach tends to increase noise while the circulation based approach tends to reduce noise since the usage of 8 velocities instead of 2 effectively has a smoothing effect. This is illustrated in Fig. 6. It can be seen that the center difference scheme is more noisy compared to the circulation based approach.

2.5 Vortex center identification

Blade tip vortices of hovering rotors are very well defined and have a single peak of vorticity, λ_2 or Q in their center, as shown in [1, 2]. In contrast, the tip vortices of lightly loaded rotors in forward flight, especially those created on the advancing side, often are very weak and hard to detect. In HHC cases inboard vortices are present that are generated in form of radially distributed vorticity without a designated center. In these cases the flow field operators show a wide spread cloud of individual peak values of comparable intensity that do not allow the decision for a discrete vortex center. In addition, these individual peaks are at different locations in each of the images.

To circumvent this problem, the area center of a flow field operator can be used to define the center of the vortical structure. Even better results are obtained when computing new scalars based on the convolution integral of the flow field operators with a specially shaped norm function. This norm function shall represent the expected distribution of the operator. The best fit of the data with this norm function result in largest scalar values of the convolution integral. As an example, the norm shape function applied to the vorticity, λ_2 or Q operator is shown in Fig. 7 (a). It represents the peak value distribution expected of the operator in the center of a vortex, expressed in terms of the index range covered by the norm function, here an array of 13x13 indices is used.

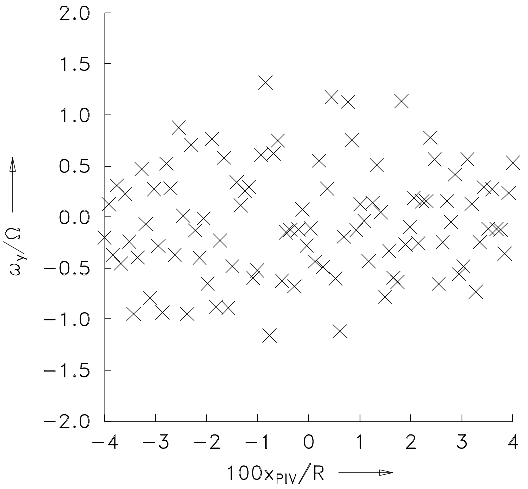

(a) center difference scheme

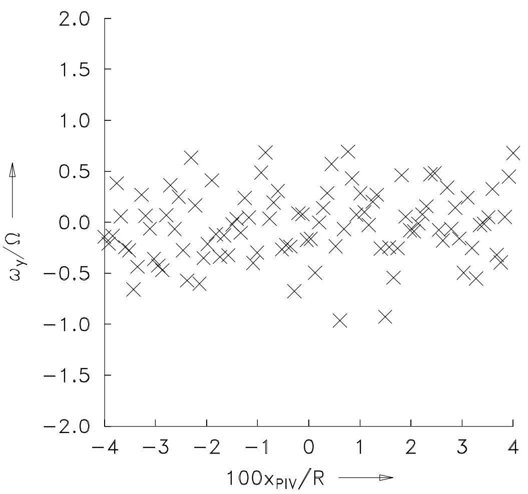

(b) circulation based

Figure 6: Effect of the method to compute derivatives on vorticity, data as in Fig. 4 at $j = 10$.

In any case, the vortex center must be expected anywhere between the grid points such that a maximum value of an operator or scalar on the grid cannot be used for the center point, rather than area center of this operator or scalar.

Another possibility to identify a vortex center, that does not need the computation of flow field derivatives, is to identify the center of swirl. This can be done by a convolution of the in-plane velocities with a discrete swirl mask as explained in [24]. Here, the swirl mask is created using a Vatistas type vortex [18] with a core radius of $2\Delta x$ and $n = 1$. The swirl mask is decomposed into its horizontal and vertical vector components. The first mask is multiplied with the u component of

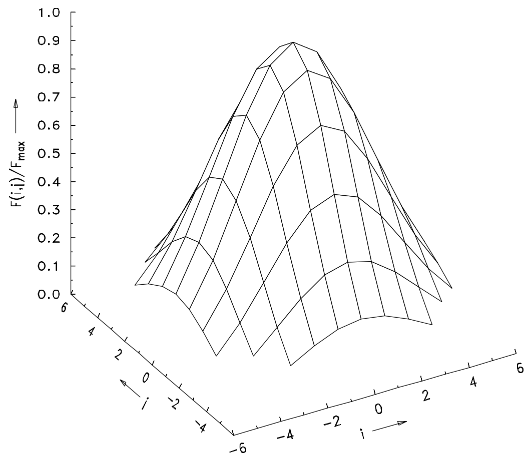

(a) Function for vorticity, λ_2 and Q.

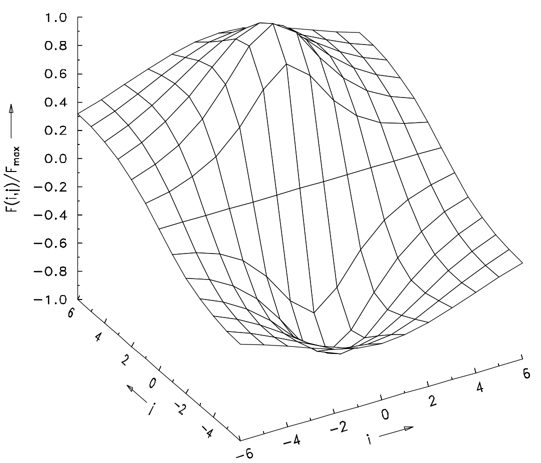

(b) Function for u and w.

Figure 7: Norm shape functions used for convolution with flow field data, index space.

the flow field and shown in Fig. 7 (b), the second mask has the same distribution as in Fig. 7 (b) but rotated by 90^o and is multiplied with the w component of the flow field.

The sum of both provide a qualitative scalar value of the rotational character of the flow and also indicate the sense of rotation, as is the case when using vorticity. In general, this swirl mask can be interpreted as a special areal wavelet, such that this convolution can also be named a wavelet analysis. The λ_2 and Q operators are insensitive to the sense of rotation and always negative in the centers of vorticity.

Results for the different methods are shown in Fig. 8. The data is from HART II, BL case, pos. 17d (vortex age of 20^o), first image. The vortex center locations are marked by a "+" sign, and the core radius identified by a circle around the center. In this case the blade tip was almost unloaded and essentially the shear layer is present, with some vortical components. In any case the extremum value (positive and negative for ω_y and convolution of u, w; negative only for λ_2 and Q operators) of the various scalars computed for the image is searched first, then the area center is computed in the vicinity of this extremum.

Since the distribution of vorticity is very noisy the identification of the center of vorticity is difficult, Fig. 8 (a). In this case several minima are present. The convolution of vorticity with a bell-shaped norm function results in the scalar field of Fig. 8 (b). Due to the convolution, the noise is widely suppressed, and essentially three negative peaks and one positive peak can be found, the latter indicates a small vortex of opposite sense of rotation.

The λ_2 and Q operators indicate vortical structures by negative values, see Fig. 8 (c) and (d). Both are in the same scalar range, but Q is slightly more noisy compared to λ_2. Three peaks are clearly marked for local centers of vorticity, the pair in the middle of the image is of stronger nature than the single peak in the left half. The convolution of λ_2 with a bell-shaped norm function results in the scalar field of Fig. 8 (e), which is very similar to the convolution of Q not shown here. Now the central point is focused and identified as the strongest event in the image. Finally, in Fig. 8 (f) the convolution of the swirl mask with the in-plane velocity field is presented. This essentially seems comparable to Fig. 8 (b), but with more emphasis on the location found in (e). Therefore, the methods in Fig. 8 (e) and (f) are found to be best suited to identify the center of vortical structures where no clear vortex can be detected.

As can be seen from the Fig. 8, the core radii identified are strongly depending on the location of the vortex center. However, the noise in individual data is affecting the identification of the core radius to some extent, but this will be alleviated using proper averaging of the data.

2.6 Conditional averaging

Due to elasticity of the support, the model was vibrating with low frequencies that were not rotor harmonics. Although these were of small nature (few mm) they were transferred to the blade tips and resulted in different vortex creation positions each revolution of the rotor. A second source of vortex motion in the images was the elasticity of the camera support structure. When shaking, the observation area was slightly different at each individual measurement. This resulted in an apparent vortex motion in the observation area.

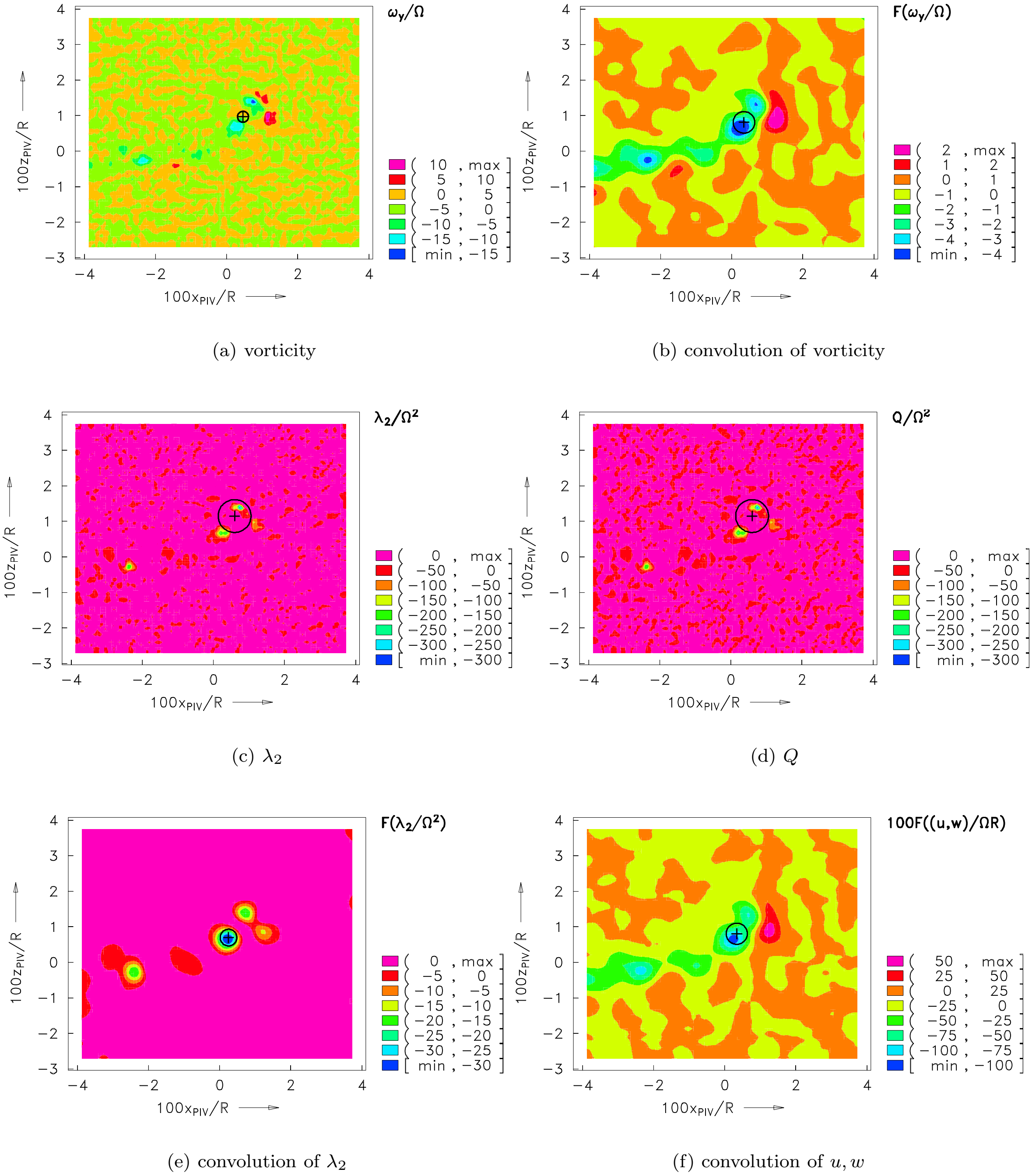

(a) vorticity

(b) convolution of vorticity

(c) λ_2

(d) Q

(e) convolution of λ_2

(f) convolution of u, w

Figure 8: Vortex center identification by area center of different scalars. Pos. 17d of Fig. 1 (b), vortex age: 20^o, first image. Vortex center at "+", the core radius is indicated as circle.

The first source of motion was independent of the measurement location, while the second source depended on the proximity of the camera tower to the shear layer of the free-stream jet. A third source of vortex center position changes was the vortex wander itself, depending on its age.

Care must thus be taken for averaging the data. A simple (ensemble) average results in artificially large core radii and low values of vorticity and is not representative for any of the individuals. This was already found in [1], where the conditional averaging was also applied, and observed in [2], where the conclusion was made that PIV is not suitable for vortex core measurements. The simple average can only be used for the average location of the vortex center and the total circulation of the vortex, which is obtained for radii far outside the core. A proper (conditional) averaging must retain the individual characteristics like peak swirl velocity and core radius but eliminate

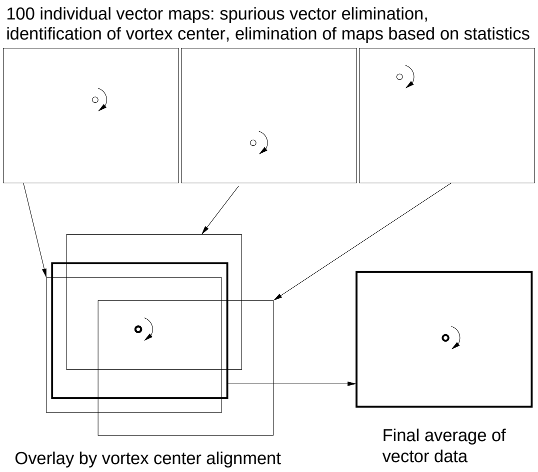

Figure 9: Conditional averaging procedure.

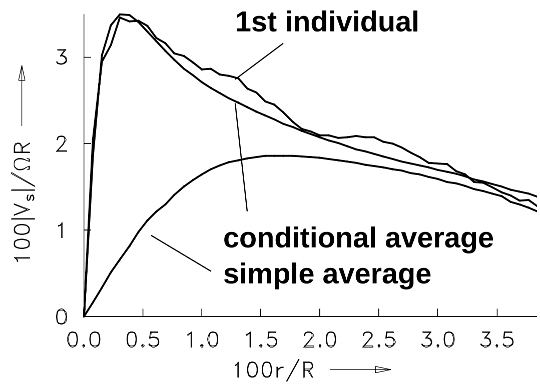

Figure 10: Effect of averaging method on swirl velocity profile, BL, pos. 23.

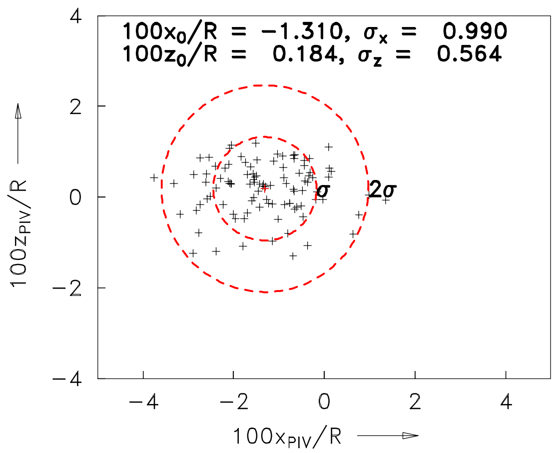

Figure 11: Scatter of vortex centers, BL, pos. 23.

the random fluctuations.

The principle of conditional averaging is shown in Fig. 9. In each of the individual images the center is first identified, then all centers are shifted to coincide with each other. A new grid is generated with its center in the center of all the individual vortices. Then, all data are interpolated and averaged in the new grid. Before this, a statistical analysis of the vortex center positions can be made, eliminating all positions that are a certain threshold away from the mean center position, for example, 2 standard deviations. This ensures that outliers are not taken into account. Additionally, the peak vorticity at the vortex center can be compared in the same way, eliminating all data that are either a certain threshold below the average, or above.

As an example for the differences of the averaging methods the swirl velocity profile of the BL case at pos. 23 (at the rear of the disk where the vortex age is almost 1.5 revolutions) is shown in Fig. 10. The simple average leads to 5 times larger apparent core radii ($r_c/R \approx 0.0175$) than the conditional average, which is very close to the individual also shown (both $r_c/R \approx 0.0035$). Also, the peak velocities at the core radius found in the simple average are only about half the value found for the conditional average or for the individual. Outside the core, the different averaging methods approach each other.

The reason for the differences is found in the scatter of vortex positions of the individual images, which is shown in Fig. 11. Due to model movements and vortex wander, the entire area of vortex center positions has a radius of 2%R, much larger than the core radius of these vortices. Therefore, a simple average cannot be used for the analysis of vortex parameters, except for its average position and the total circulation.

Additionally, in Fig. 12 the number of images available for averaging at each grid point is shown. The total number of images is 100, but due to the statistics based elimination process, 9 images (where the vortex center was found very far away from the mean center position) were removed. In this case the vortex is found virtually in all images, mostly to the left side of the window (see Fig. 11), since the number of images per grid point reduces significantly to the left of the figure.

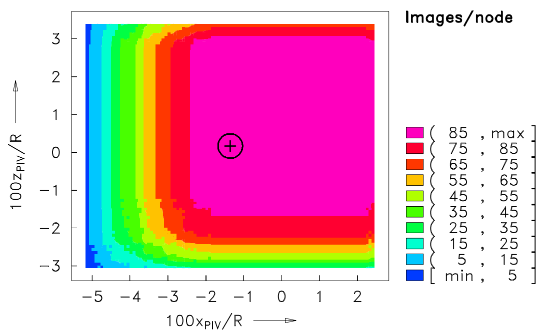

Figure 12: Images per grid node available for averaging, BL, pos. 23.

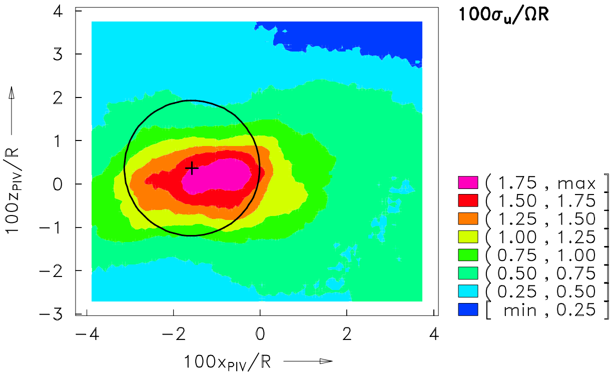

(a) $\sigma(u)$, simple average

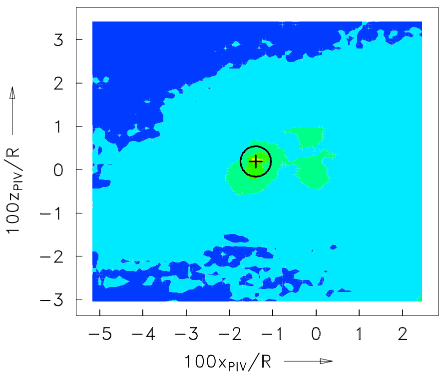

(b) $\sigma(u)$, conditional average

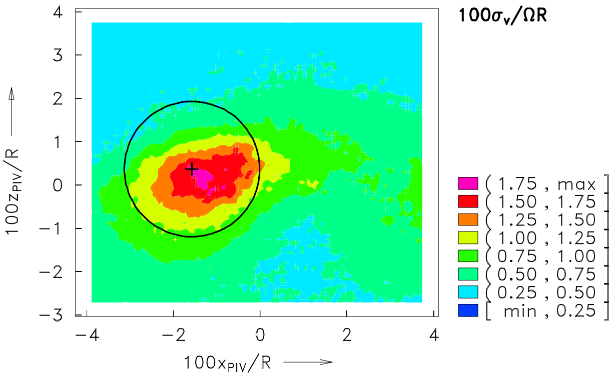

(c) $\sigma(v)$, simple average

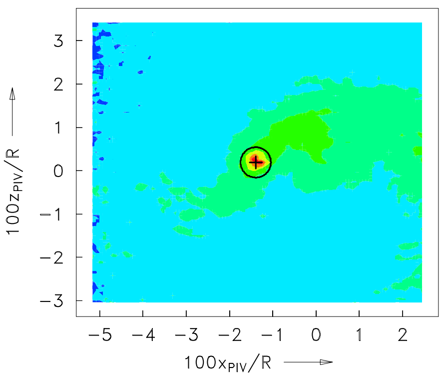

(d) $\sigma(v)$, conditional average

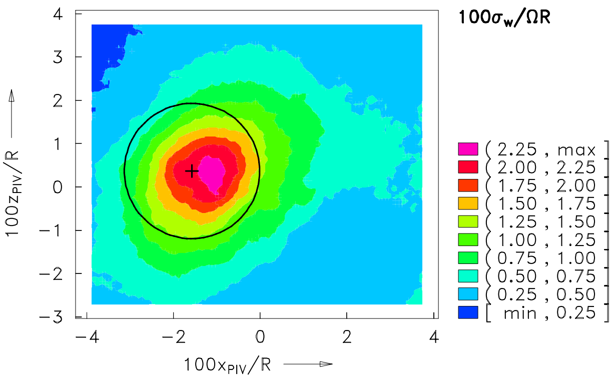

(e) $\sigma(w)$, simple average

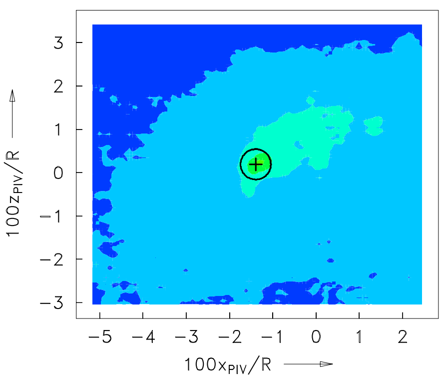

(f) $\sigma(w)$, conditional average

Figure 13: Effect of averaging method on standard deviation of flow components, BL, pos. 23.

The importance of conditional averaging can also be illustrated by the standard deviation of the flow components at each node of the grid. This is shown in Fig. 13 (a), (c) and (e) for the component u, v and w of the simple averaging method, and in (b), (d) and (f) for the conditional averaging. Again, pos. 23 of Fig. 1 is taken here. In all components the simple average has a much wider range of scatter compared to the conditional average, which is due to the scatter of vortex center positions in the individual images. Once the centers are aligned, the fluctuation of flow components is significantly smaller. The vortex core radii are also much smaller as indicated by the circles in the graphs, which represents the result already shown in Fig. 10. In any case the maximum scatter is obtained in the vortex center itself, with the largest deviations for the cross-flow component v. This is expected since this component contains the largest measurement errors.

2.7 Mean velocity elimination

The mean velocity components are to be identified for all three components and subtracted from the flow field for analysis of vortex properties. It must be differentiated here between average and mean velocity. The average of a flow component of a PIV image is defined as the sum of this component at all grid points, divided by the number of grid points. The mean flow velocity is defined by the undisturbed flow. Without a vortex in the flow average and mean velocity are identical.

In cases where a vortex is not perfectly centered in an image (which is mostly the case) the swirl velocity field of this vortex biases the computation of the mean in-plane velocities. This is most obvious when the vortex center is located at one of the image borders and the swirl velocity field of only one side of the vortex dominates the figure. In any case, the axial velocity field of a vortex complicates the computation of the mean cross-flow velocity. The problem is even more complex when the vortex axis is inclined with respect to the measurement plane and part of the swirl velocities are contained in the cross-flow, as well as part of the axial velocity of the vortex becomes part of the in-plane velocity field.

Based on the assumption that the vortex convects with the mean velocity, the in-plane components u_{mean} and w_{mean} can be computed from the velocities found in the vortex center. This is not the case for the out-of-plane component v since an axial flow is expected in the vortex core with its maximum in the vortex center, and asymptotically approaching zero outside the core radius. Therefore, v_{mean} must be computed from the flow field sufficiently far outside the vortex core radius.

An example for the identification and elimination of the mean in-plane velocities is given in Fig. 14 for the simple average of the BL case, pos. 17 (here the vortex age is about 27^o). After removal of the mean in-plane velocities, the vortex core in the center of the figure (indicated by the circle) and the shear layer in the lower left quarter of the figure exhibit the largest in-plane velocities, but in the center of the vortex (marked by the "+" sign) the velocity is zero.

In cases where the shear layer of the blade creating the vortex (or another blade that just passed the observation window) is present, it contributes a significant out-of-plane or cross-flow velocity and biases the computation of v_{mean}. To identify these areas, again the method of convo-

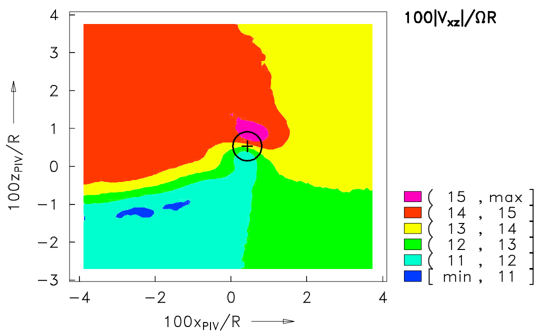

(a) In-plane velocities magnitude.

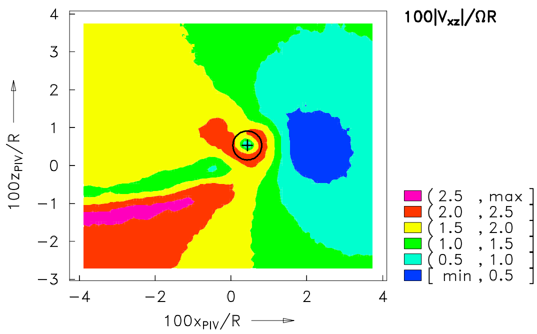

(b) $u_{mean} = -0.133\Omega R$ and $w_{mean} = 0.023\Omega R$ subtracted.

Figure 14: Identification and elimination of the mean in-plane velocities, BL, pos. 17.

lution can be used with the same norm function as used for the flow field operators and applied to the out-of-plane velocity component, since the thickness of these shear layers usually is small. Any locations where the scalar value of this convolution is exceeding a certain threshold indicate areas not to be used for computation of v_{mean}. A result of this method is given in Fig. 15 for the same case as used in Fig. 14. Therein the shear layer contributes even more cross-flow velocities than the center of the tip vortex itself. However, the mean cross-flow component is identified from all flow outside the shear layer and outside the vortex core such that the outer areas are close to zero cross-flow after subtraction of the mean components.

Note that $-u_{mean}\cos 30^o - v_{mean}\sin 30^o = 0.155\Omega R$, which is essentially the wind speed ($\mu = 0.151$) plus the horizontal velocity induced by the rotor at this location. The difference of $0.004\Omega R = 0.87 m/s$ is little more than the accuracy of the wind tunnel jet velocity of $\pm 0.4 m/s$. The component lateral to the wind tunnel flow results in $-v_{mean}\cos 30^o + u_{mean}\sin 30^o = 0.003\Omega R$ and is small compared to the other directions.

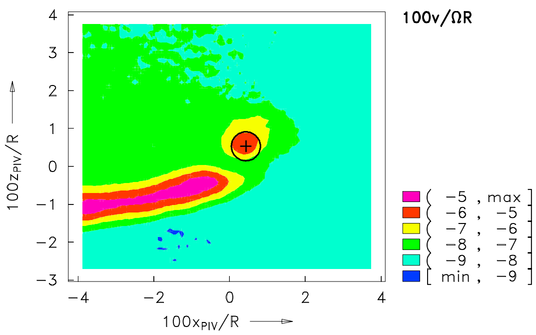

(a) Cross-flow velocities.

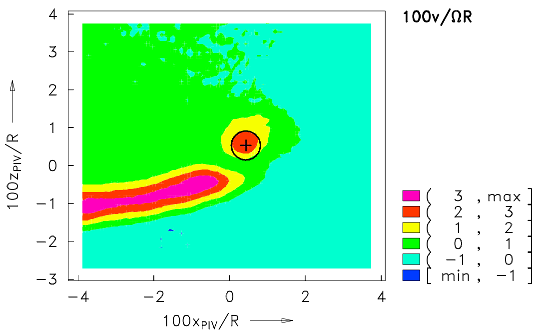

(b) $v_{mean} = -0.08\Omega R$ subtracted.

Figure 15: Identification and elimination of the mean cross-flow velocity, BL, pos. 17.

2.8 Rotation into the vortex axis system

Due to a fixed angle of view of the PIV systems into the three-dimensional vortex system of the rotor, the measurement plane was never orthogonal to the vortex axis. A correct analysis of the vortex parameters can only be made in the vortex axis system. Thus, the inclination angles between the measurement plane and the vortex axis have to be identified.

The assumption is made that the vector field does not change in a small volume along the vortex axis. In this case the measurement window can be shifted along the vortex axis without change of the velocity vectors therein. The rotation scheme is illustrated in Fig. 16. Two rotation angles are identified, the angle about the x-axis and the angle about the z-axis. First the rotation about z is performed, then the rotation about x. The final grid in a plane normal to the vortex axis is a sheared grid.

Based on the assumption that in the vortex axis system the out-of-plane velocity distribution is rotational symmetric, different methods were developed to identify these rotation angles. First, the out-of-plane and swirl velocity components at

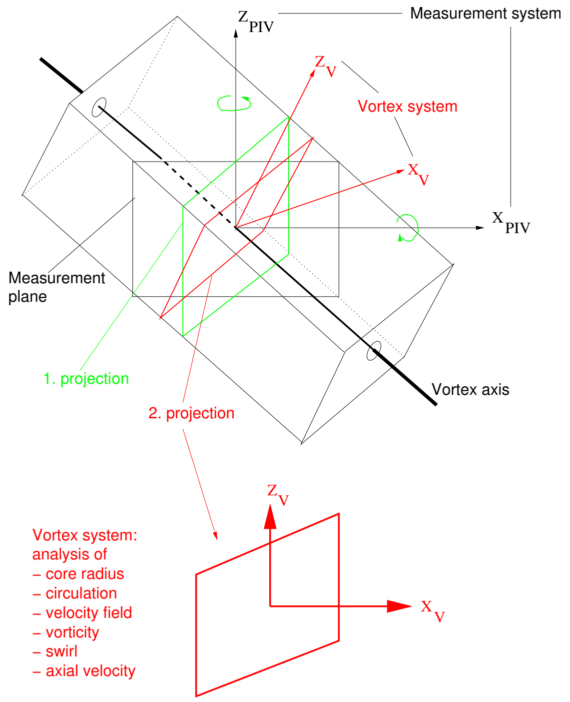

Figure 16: Rotation from the measurement plane into the vortex axis system.

the core radius, identified from a horizontal and a vertical cut through the vortex center, are used. Second, the global out-of-plane velocity gradients with respect to x and z are identified and used for a guess of rotational angles.

Using these angles the coordinates and velocity vectors are rotated into the assumed vortex axis system, usually leading to a sheared grid as depicted in Fig. 16. The resulting flow field is again analysed for the cross-flow distribution using any of the methods to identify a vortex center, and the procedure is repeated until the remaining rotation angles are below a certain threshold, for example 1^o. Then, the analysis of vortex properties can be made. Usually the vortices appear elliptical in the original unrotated data, while they appear circular in the rotated data.

An example for the effect of rotation into the vortex axis system is shown in Fig. 17 for the simple average of the BL case, pos. 29, where the vortex is cut by the PIV measurement plane at an angle of $\beta_z \approx 45^o$ when considering Fig. 1. The unrotated data in (a) show some ellipticity of the in-plane velocities (vector field) and also in the cross-flow, where global gradients exist in the areas outside the vortex core. The identification of rotation angles based on the cross-flow in the core radius and the swirl leads to angles of $\beta_z = -45^o$ about the vertical axis and of $\beta_x = 3^o$ about the horizontal axis.

The resulting velocity field after rotation is also shown in Fig. 17 (b). Due to the sequence of ro-

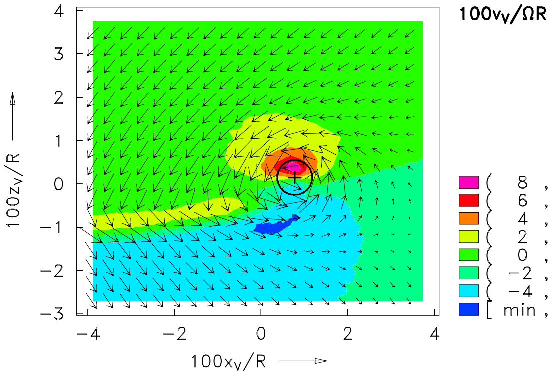

(a) Measurement plane.

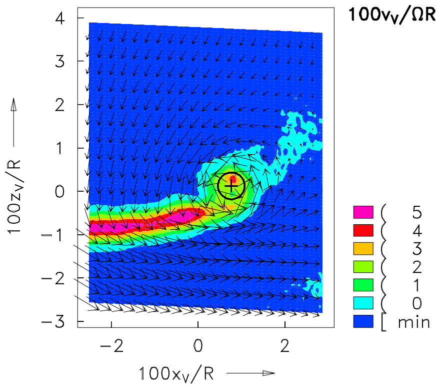

(b) Vortex axis system, rotated by $\beta_x = 3^o$ and $\beta_z = -45^o$.

Figure 17: Effect of rotation into the vortex axis system on the velocity field, case BL, pos. 29.

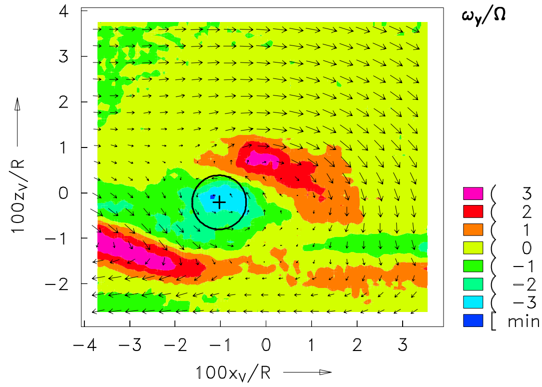

(a) original data

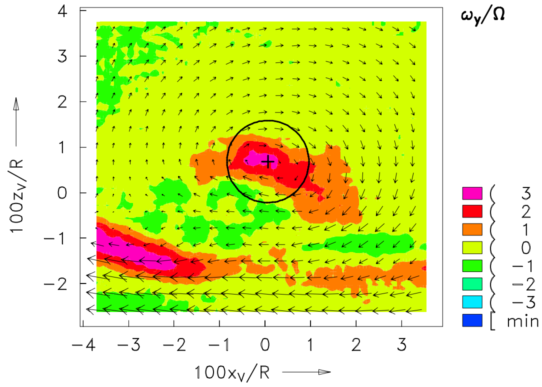

(b) counter-rotating vortex removed

Figure 18: Elimination of disturbing structures. BL, pos. 47 of Fig. 1, simple average.

tation the grid is sheared, but the distribution of the in-plane velocity vectors is very round now compared to the unrotated data. Also, the cross-flow is zero in the field outside the vortex, and in the vortex center a peak is present as expected. A strong shear layer to the left of the tip vortex is clearly visible now.

After rotation into the vortex system the effective measurement area is smaller than the raw data area, and the grid effective spacing is smaller. In these cases the angle of the measurement plane relative to the vortex axis is effectively increasing the spatial resolution of the measurement.

2.9 Elimination of secondary structures

Based on the superposition principle, vortices and vortical shear layers from blades passing the measurement window are identified and numerically removed from the image such that the vortex of interest remains almost unaffected. Thereafter, its parameters can be identified without being biased by disturbing structures.

An example is given in Fig. 18 where in (a) two vortices of opposite sense of rotation are close to each other, and both are affecting the other vortex flow field adversely. After elimination of one of these the remaining vortex is clearly unaffected by other structures and its parameters can be identified.

2.10 Identification of vortex parameters

The identification of the swirl and the axial velocity profiles, the core radius and the circulation is often hindered by other flow structures in close proximity of the vortex of interest. These are shear layers with vorticity and additional vortices shed by other blades just passing the measurement window, especially where BVI takes place.

Using a best fit of a Vatistas vortex swirl model

[18] the parameters describing the vortex are identified. This model is written in terms of the maximum swirl velocity $V_{s,max}$ at the core radius r_c, the shape parameter n that describes the distribution of vorticity (and therewith the distribution of λ_2 and Q, see also App. A) and the radial distance from the vortex center. The development of vortex circulation, and thus the fraction of total circulation at the core radius, is connected to the swirl velocity profile as well. All relations for the Vatistas vortex are given in the appendix. Note that all varables are made non-dimensional as described in App. A.

$$\begin{aligned} V_s &= V_{s0}\frac{r}{(1+r^{2n})^{1/n}} \\ V_{s0} &= V_{s,max}2^{1/n} = \frac{\Gamma_v}{2\pi r_c} \end{aligned}$$

Alternatively, the Lamb-Oseen [26, 25] or Newman [27] vortex can be fitted to the data. These are also written in terms of $V_{s,max}$ and r_c, but the radial distribution function is different and a factor α of an exponential function defines the shape. Expanding the parameter α to the inclusion of the vortex age ψ_v the Hamel-Oseen [28] model can be used as well.

$$\begin{aligned} V_s &= V_{s0}\frac{1-e^{-\alpha r^2}}{r} \\ V_{s0} &= \frac{V_{s,max}}{1-e^{-\alpha}} = \frac{\Gamma_v}{2\pi r_c} \end{aligned}$$

Vatistas model is used here, since with the shape parameter n a wide range of swirl shapes can be defined, covering the Scully vortex ($n = 1$), the Lamb-Oseen vortex ($n \approx 2$) or the Rankine vortex ($n = \infty$). When the data are cleaned from spurious vectors, mean values of the flow subtracted and rotated into the vortex axis system, the distribution of swirl velocities of all vectors is fitted with the Vatistas model using a least squares error method. As an example, in Fig. 5 such a best fit is shown. The best fit is performed to a radial extension of 2-3 core radii. As a result, the core radius was found at $r_c = 0.0122R$, the maximum swirl velocity as $V_{s,max} = 0.0919\Omega R$, and the shape parameter as $n = 1.979$. It can be seen that the best fit with these parameters (red curve) perfectly represents the data.

3 Virtual 3C-PIV

For validation of the analysis methodology a numerical experiment was performed. An area as large as the DLR measurement window was created and a Vatistas type of vortex was used to generate a vector field. The resolution of the vector field was selected the same as most of the DLR data had with 100 vectors in x and 85 vectors in y direction. Four different cases were generated, where in any case the vortex center is between the grid nodes. The flow field of all three components of each case is shown in Fig. 19.

1. The vortex is weak and orthogonal to the grid without any noise.
2. The vortex is strong and orthogonal to the grid, but random noise of 10% of the maximum velocity is added to each component of all vectors.
3. The vortex is weak and significantly inclined with respect to the grid without any noise.
4. The vortex is strong and significantly inclined with respect to the grid, and random noise of 10% of the maximum velocity is added to each component of all vectors.
5. Two vortices of opposite sense of rotation are present close to each other.

While these four cases are representing the flow field of only one vortex the fifth case shown in Fig. 20 (vorticity is also shown) is more difficult since the analysis of one of both vortices is biased by the presence of the other vortex. Therefore, one of the vortices must be eliminated first in order to analyse the other. The vorticity distribution of case 5 indicates that both vortices are close together and of comparable strength in terms of their vorticity, but of different strength in terms of their circulation. They have an opposite sense of rotation, indicated by the sign of vorticity. Additionally, in order to further complicate the analysis, random noise was added to all flow components.

3.1 Case 1

This is the most primitive test case since the vortex is normal to the measurement plane and no noise is added. Tab. 2 compares the parameters identified by the methodologies described in the section before with those used to create the vector field. In general excellent agreement is found for all parameters.

3.2 Case 2

Case 2 is more difficult since random noise is involved. Therefore, the parameters identified show somewhat larger differences to the data used to generate the vector field, see Tab. 3. Nevertheless, the overall agreement is still very good.

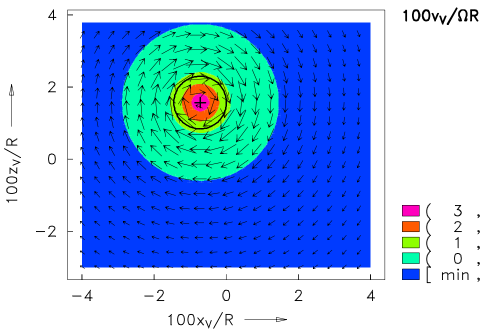

(a) Case 1: orthogonal, no noise.

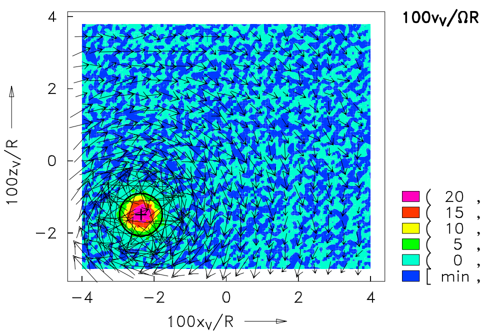

(b) Case 2: orthogonal, with noise.

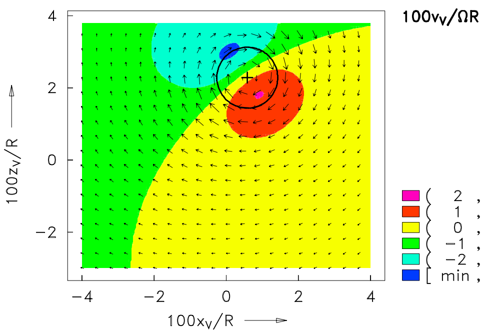

(c) Case 3: inclined, no noise.

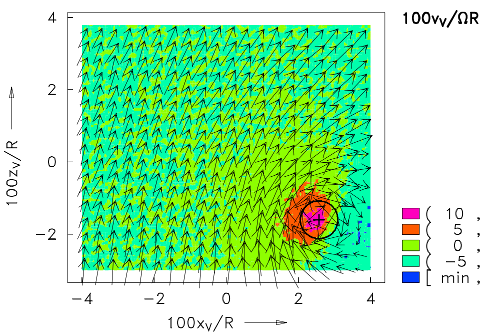

(d) Case 4: inclined, with noise.

Figure 19: Virtual 3C-PIV data, one vortex.

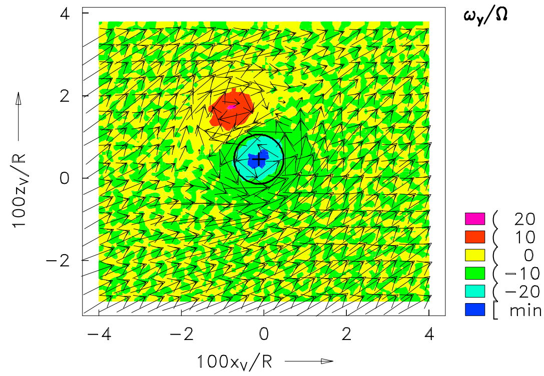

(a) Vorticity.

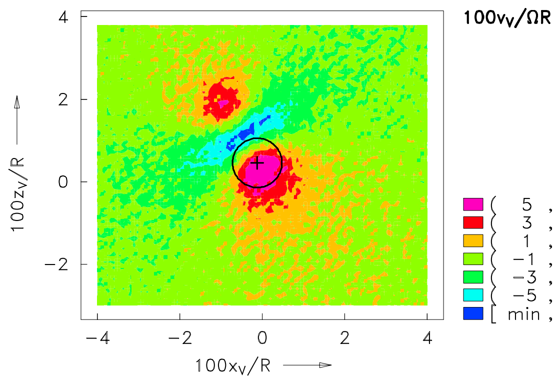

(b) Cross-flow.

Figure 20: Virtual 3C-PIV data, case 5: two vortices, both inclined, with noise.

Parameter	data	identification
$100u_{mean}/\Omega R$	15.100	15.097
$100v_{mean}/\Omega R$	0.000	0.135
$100w_{mean}/\Omega R$	3.500	3.553
$100v_0/\Omega R$	3.528	3.375
$100x_0/R$	-0.719	-0.725
$100z_0/R$	1.566	1.565
$100r_c/R$	0.727	0.728
$100\Gamma_v/\Omega R^2$	0.429	0.425
$100V_{s,max}/\Omega R$	5.592	5.583
ω_{y0}/Ω	12.918	12.828
n	1.337	1.321

Table 2: Results of parameter identification for data of case 1.

3.3 Case 3

The vortex generated is now significantly inclined with respect to the virtual PIV data field, but the data are clean without any noise. Results are shown in Tab. 4. The agreement of the parameters identified is as good as for the unrotated case, although the rotation angles are larger than 20^o

Parameter	data	identification
$100u_{mean}/\Omega R$	15.100	14.844
$100v_{mean}/\Omega R$	0.000	0.050
$100w_{mean}/\Omega R$	3.500	3.336
$100v_0/\Omega R$	23.913	25.895
$100x_0/R$	-2.368	-2.361
$100z_0/R$	-1.489	-1.495
$100r_c/R$	0.593	0.592
$100\Gamma_v/\Omega R^2$	0.911	0.908
$100V_{s,max}/\Omega R$	18.354	18.239
ω_{y0}/Ω	41.231	37.597
n	2.417	2.375

Table 3: Results of parameter identification for data of case 2.

Parameter	data	identification
$\beta_x/^o$	22.700	23.074
$\beta_z/^o$	-37.100	-37.312
$100u_{mean}/\Omega R$	14.984	14.999
$100v_{mean}/\Omega R$	3.072	3.161
$100w_{mean}/\Omega R$	2.509	2.463
$100v_0/\Omega R$	0.833	0.811
$100x_0/R$	0.549	0.550
$100z_0/R$	2.325	2.330
$100r_c/R$	0.722	0.720
$100\Gamma_v/\Omega R^2$	0.207	0.207
$100V_{s,max}/\Omega R$	3.006	3.003
ω_{y0}/Ω	6.320	6.357
n	1.661	1.643

Table 4: Results of parameter identification for data of case 3.

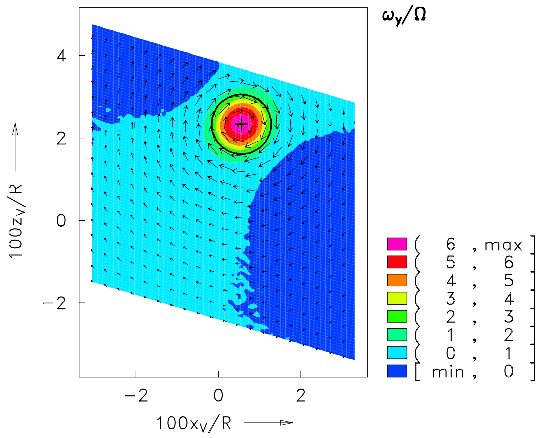

(a) In-plane velocities and vorticity.

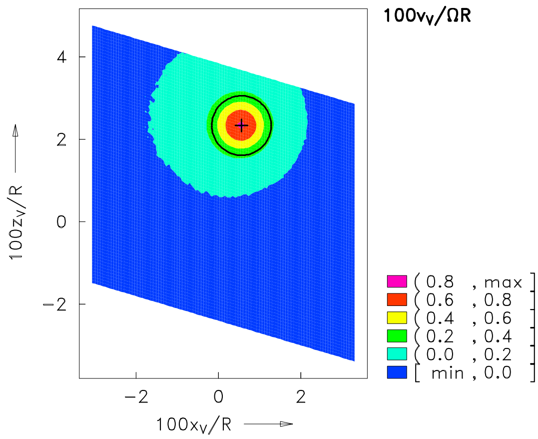

(b) Cross-flow velocity.

Figure 21: Flow field after rotation into the vortex axis system, case 3.

in β_x and more than 35^o in β_z. This indicates the rotation methodology works perfectly with such clean data.

The distribution of in-plane velocity vectors and vorticity, together with the cross-flow distribution, is shown in Fig. 21. Compared to the original data in Fig. 19 (c) the cross-flow component is in the range of zero for a distance of two core radii or more outside the vortex center, with a peak of vortex axial flow in the center itself and and the vortex appears now perfectly round. The closeness to the upper image border does not adversely affect the analysis.

3.4 Case 4

More realistic, in this case not only the vortex is inclined and very close to the border, but also random noise is added to this case. The comparison of identified parameters with those used to create the data is given in Tab. 5. In general, the agreement is very good as for the unrotated data with noise (case 2). In β_z a difference of almost 4^o is found, but for the analysis of core radius or peak swirl velocity errors of up to 10^o seem to be acceptable.

The distribution of in-plane velocity vectors and vorticity, together with the cross-flow distribution, is shown in Fig. 22. Compared to the original data in Fig. 19 (d) the vortex appears now perfectly round, and the cross-flow component is in the range of zero for two core radii or more outside the vortex center, with a peak of vortex axial flow in the center itself. Again, the closeness to the upper image border does not adversely affect the analysis.

3.5 Case 5

For analysis of one of the two vortices the other was eliminated using the method described in the section before. Thereafter the vortex of interest is focused, the rotation algorithm applied, and parameter identification started in the final grid.

Parameter	data	identification
$\beta_x/^o$	-37.400	-36.465
$\beta_z/^o$	17.800	14.099
$100u_{mean}/\Omega R$	10.143	10.599
$100v_{mean}/\Omega R$	-11.012	-9.937
$100w_{mean}/\Omega R$	-4.014	-3.610
$100v_0/\Omega R$	14.612	15.445
$100x_0/R$	2.683	2.680
$100z_0/R$	-1.651	-1.637
$100r_c/R$	0.453	0.459
$100\Gamma_v/\Omega R^2$	0.544	0.515
$100V_{s,max}/\Omega R$	9.429	9.272
ω_{y0}/Ω	42.191	44.086
n	0.981	0.843

Table 5: Results of parameter identification for data of case 4.

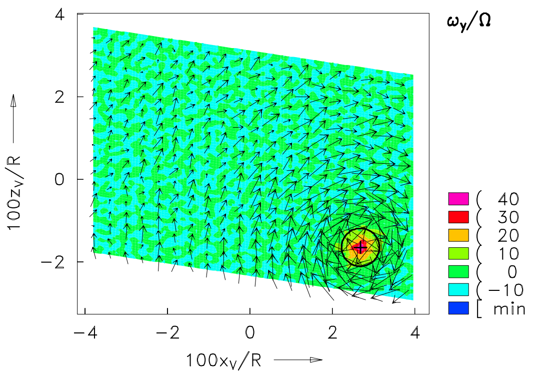

(a) In-plane velocities and vorticity.

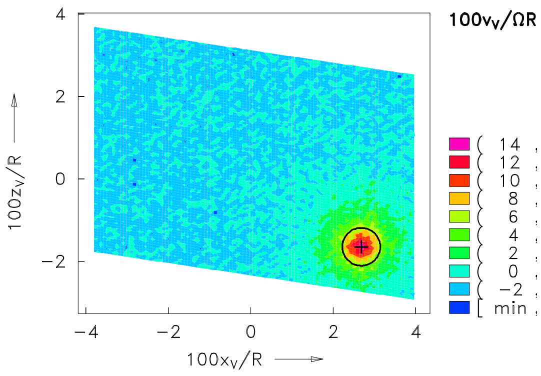

(b) Cross-flow velocity.

Figure 22: Flow field after rotation into the vortex axis system, case 4.

Results obtained for both of the vortices are given in Tab. 6. In general, the vortex parameters are identified with sufficient accuracy.

Surprisingly, the major differences are found in the computation of the mean velocities. This is visible in the in-plane velocity vector fields of the two vortices shown in Fig. 23 and Fig. 24. Due to the close proximity of both vortices the identification of the parameters of the vortex to be eliminated is biased by the other vortex. Therefore, remnants of the vortex to be eliminated are still present in the center of the remaining vortex.

In the cross-flow distribution of both vortices shown in Fig. 23 and Fig. 24 the axial velocity field of the second vortex is always visible, since the algorithm does only subtract the in-plane velocities and not (yet) the axial flow field of a vortex.

To proper identify the mean velocities of the entire field, the vortex central point can be set manually to any location, for example far outside the two vortices, and the angles to rotate the image into the vortex axis system were manually set to the values listed in Tab. 6. The result is given in Tab. 7, and now good agreement is found for these as well. This proves the assumption that the vortex to be eliminated in either of Fig. 23 and Fig. 24 was not completely enough removed from the flow field.

Parameter	data	identification
	Vortex 1	
$\beta_x/^o$	-20.000	-16.554
$\beta_z/^o$	30.000	27.015
$100u_{mean}/\Omega R$	12.990	2.960
$100v_{mean}/\Omega R$	-8.245	-3.045
$100w_{mean}/\Omega R$	0.724	1.331
$100v_0/\Omega R$	7.036	5.877
$100x_0/R$	-0.719	-0.738
$100z_0/R$	1.574	1.594
$100r_c/R$	0.600	0.563
$100\Gamma_v/\Omega R^2$	0.500	0.489
$100V_{s,max}/\Omega R$	8.355	8.252
ω_{y0}/Ω	22.105	21.276
n	1.500	1.858
	Vortex 2	
$\beta_x/^o$	-20.000	-16.198
$\beta_z/^o$	30.000	28.166
$100u_{mean}/\Omega R$	12.990	4.868
$100v_{mean}/\Omega R$	-8.245	-4.697
$100w_{mean}/\Omega R$	0.724	2.171
$100v_0/\Omega R$	10.132	8.314
$100x_0/R$	-0.202	-0.173
$100z_0/R$	0.562	0.543
$100r_c/R$	0.600	0.588
$100\Gamma_v/\Omega R^2$	0.600	0.563
$100V_{s,max}/\Omega R$	10.026	9.877
ω_{y0}/Ω	26.526	25.933
n	1.500	1.598

Table 6: Results of parameter identification for data of case 5.

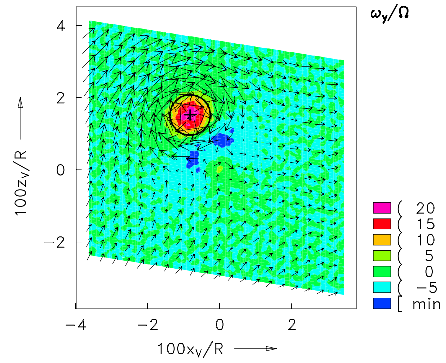

(a) Vorticity

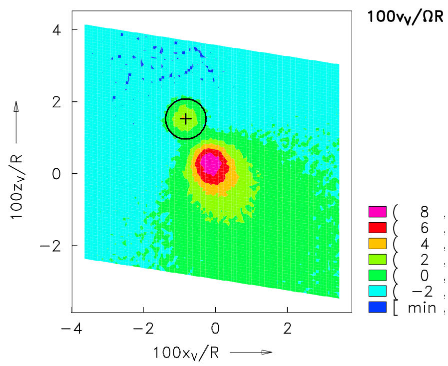

(b) Cross-flow

Figure 23: Flow field after rotation into the vortex axis system, case 5, vortex 1.

Parameter	data	identification
$u_{mean}/\Omega R$	0.130	0.135
$v_{mean}/\Omega R$	-0.082	-0.076
$w_{mean}/\Omega R$	0.007	0.012

Table 7: Mean flow velocities, case 5.

For this case the velocities after subtraction of the mean flow components are given in Fig. 25 and now the vectors far enough away from the vortices exhibit the remaining noise, and the cross-flow is essentially zero there.

4 Application to HART II data

Selected positions in Fig. 1 are presented in terms of raw data, processed data of an instantaneous image, simple and conditional averaged data, vortex wander, rotation into the vortex axis system, and identification of vortex parameters using a best fit to a Vatistas type vortex.

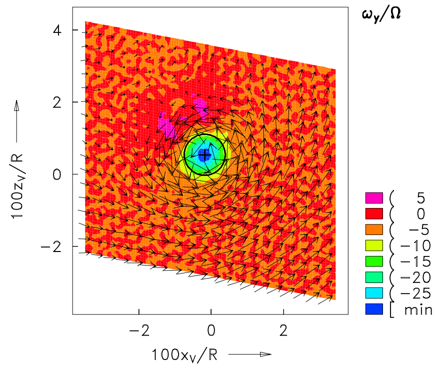

(a) Vorticity

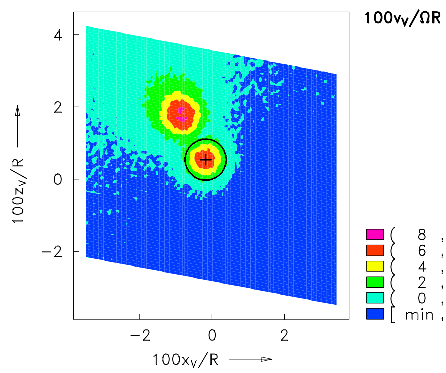

(b) Cross-flow

Figure 24: Flow field after rotation into the vortex axis system, case 5, vortex 2.

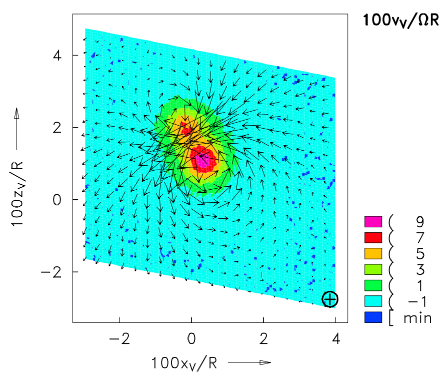

Figure 25: Flow field after rotation into the vortex axis system, case 5.

4.1 Hover

Since most of the experimental work done so far was applied to the hover case this is first used for application of the methods described. The vortex was measured at pos. 17h of Fig. 26, where in this case the blade position was at $\psi = 180^o$ and the measurement location at $\psi = 136^o$, such that the vortex age is $\psi_v = 44^o$.

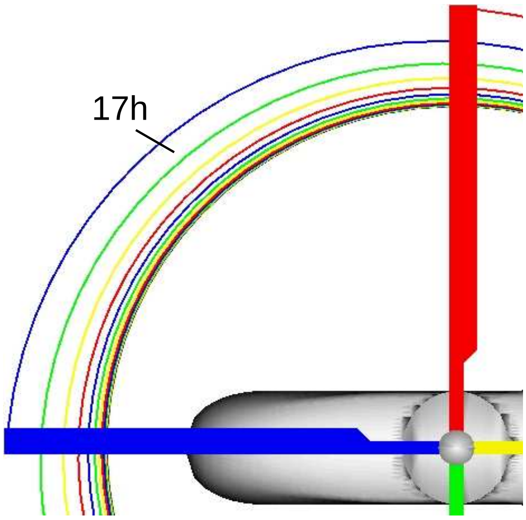

Figure 26: Location of tip vortex measurement in hover.

4.1.1 Individual data

First, the set of 100 individual images are processed separately and the results analysed statistically. Images with a vortex center found more than two standard deviations away from the mean center position are removed from the analysis, these are 14 of 100. In Fig. 27 the statistics for the remaining 86 images are given. In (a) the position of vortex centers are shown. They have an average standard deviation of $0.0013R = 0.022c = 2.7mm$ in x-direction and almost twice as much in vertical direction, which is the range of the vertical positions of the blade tip. In (b) the peak vorticity in the vortex center is shown, the standard deviation is 17% of the average value (AV). At first glance this appears too large, but it must be recalled that the vorticity is based on flow field derivatives and any measurement error is magnified by differentiation.

The angles about the x- and the z-axis needed to rotate the vector field into the vortex axis are given in Fig. 27 (c) and (d), respectively. In both cases the standard deviation is $\pm 4^o$ about the AV, which appears reasonable. The core radii found are shown in (e) with a standard deviation of 9% of the AV, and the swirl velocity shape parameter n of the Vatistas model is in (f). The standard deviation here is 14% of the AV, however, the sensitivity of the swirl profile to this parameter is not large. In (g) the maximum swirl velocities are shown, the standard deviation is 6% of the AV. The peak of cross-flow velocity is shown in (h). Here the variation is larger, which is due to four individual images where the peak is negative while in all other images it is positive. These four cases represent outliers which were not removed from the data set.

Fig. 28 (a) shows the horizontal velocity profile in a vertical cut through the individual vortex center, and (b) the vertical velocity profile in a horizontal cut. These profiles coincide very well and represent the repeatability of the measurements and the appropriateness of vortex center identification.

4.1.2 Conditional averaged data

Almost no rotation about the x-axis of the measurement plane is needed for rotation into the vortex axis system ($\beta_x = 0.3^o$), which means the vortex axis orientation is about parallel to the rotor disk at this early stage of the wake. A rotation of $\beta_z = -25^o$ about the vertical axis is found. 14^o of this angle accounts for the angle between the PIV plane orientation (150^o) and the azimuth of the measurement (136^o), see Fig. 26. The remaining angle of 11^o represents the effect of radial contraction of the tip vortex right after its creation.

Results for both the data in the measurement plane and after rotation into the vortex axis system are shown in Fig. 29. The peak vorticity is found about 20% higher in the vortex axis system, and the effect of rotation is mainly a slight compression of the x-axis, while the vector field looks comparable in both diagrams (a) and (b). More differences are found in the cross-flow distribution shown in Fig. 29 (c) for the measurement plane and (d) for the vortex axis system. Due to the vortex axis inclination with respect to the measurement plane the large swirl velocity becomes part of the cross-flow, with components at the core radius towards the observer in the lower region and away from the observer at the upper region. After rotation into the vortex axis system, only the axial velocity of the vortex is retained, which is directed towards the blade that created the vortex, see Fig. 29 (d). All the area outside the vortex has almost no cross-flow component.

In Tab. 8, the results of parameter identification are given. At this age the vortex has a maximum swirl velocity of almost 25% of the tip speed and a core radius of little more than 5% chord, which is in good agreement with LDV data presented in [2] and [29]. Both are also in perfect agreement with the average of the individual data shown in Fig. 27. At this early stage of the vortex age the peak axial velocity in the vortex center is found to be 18% of the tip speed directed towards the generating blade.

4.1.3 Simple averaged data

The analysis results of the simple averaged (SA) data, also rotated into the vortex axis system, are given in Tab. 8 as well. They have to be compared with the data from the conditional average. Both

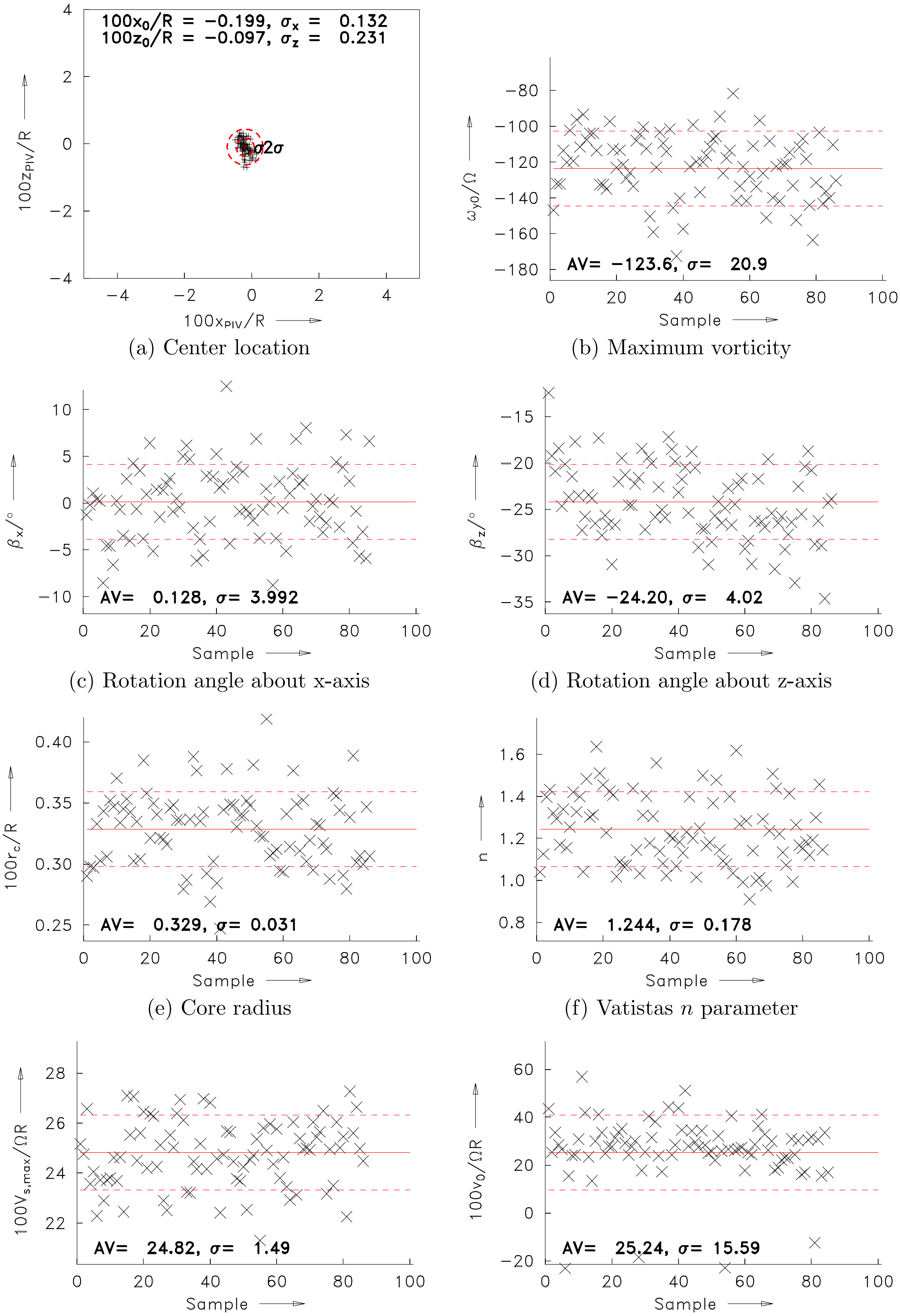

(a) Center location
(b) Maximum vorticity
(c) Rotation angle about x-axis
(d) Rotation angle about z-axis
(e) Core radius
(f) Vatistas n parameter
(g) Maximum swirl
(h) Maximum cross-flow

Figure 27: Analysis of individual data, hover, $\psi_v = 44^o$.

rotation angles agree within an accuracy of 1^o, which indicates the independence of the methodology on the method of averaging. The angles agree also well with the average of the individual data given in Tab. 27 (c) and (d).

The maximum vorticity of the simple averaged data is only half of the value of the conditional average, which represents the effect of not account-

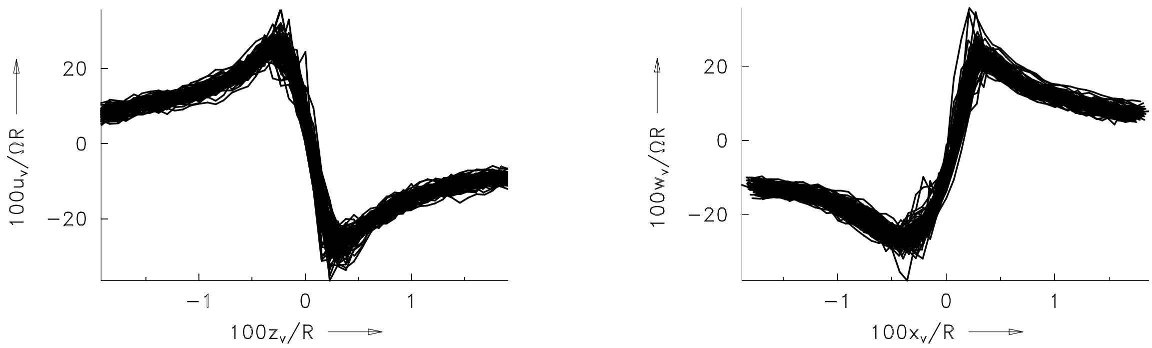

(a) Vertical cut (b) Horizontal cut

Figure 28: Analysis of individual data, hover, $\psi_v = 44^o$ - continued.

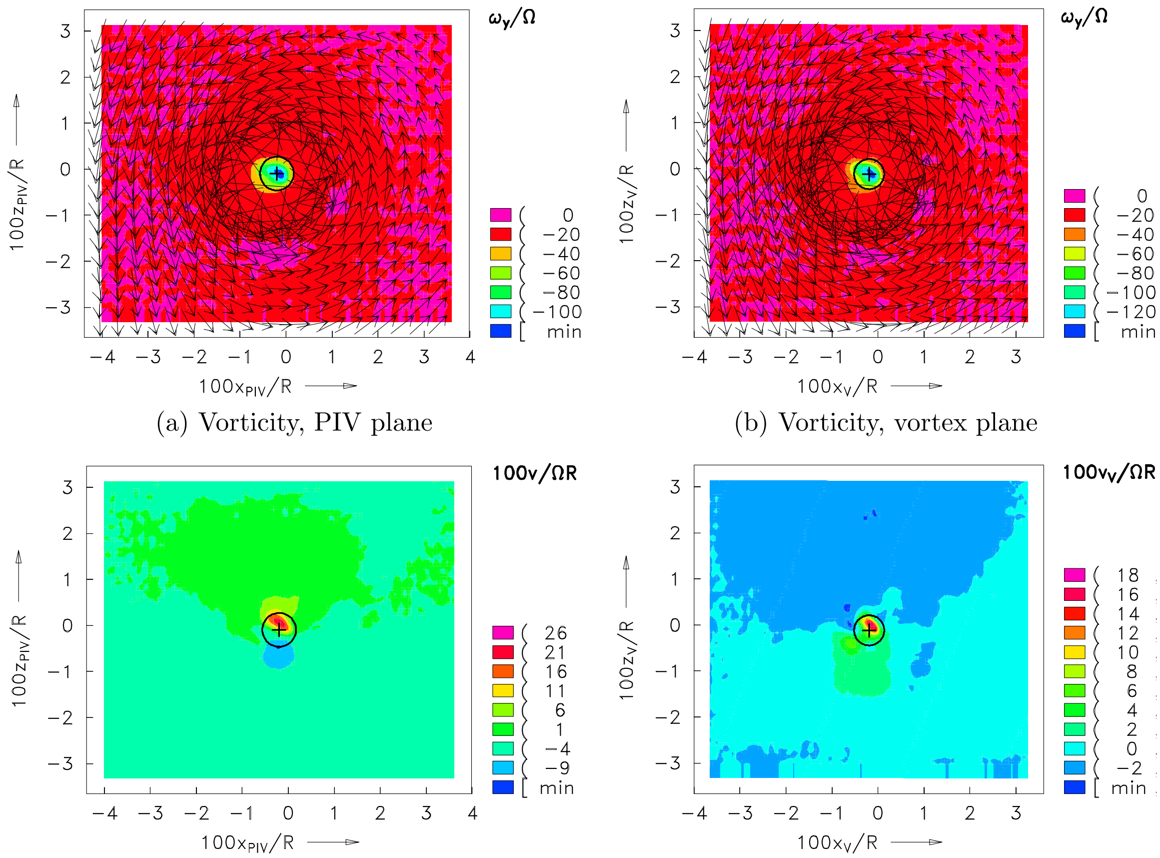

(a) Vorticity, PIV plane (b) Vorticity, vortex plane

(c) Cross-flow, PIV plane (d) Cross-flow, vortex plane

Figure 29: PIV data of a hover case in the measurement plane and rotated into the vortex axis system, pos. 17h of Fig. 26, $\psi_v = 44^o$.

ing for the individual center locations. This enlarges the core radius as well, and also reduces the peak value of axial velocity to 70% of the individual or the conditional average data. Again, the swirl shape parameter n is less sensitive to the method of averaging.

4.2 BL case, retreating side

Pos. 52 of Fig. 1 is selected here, where the blade position was at $\psi = 290^o$ and the measurement location at $\psi = 256^o$, such that the vortex age is $\psi_v = 34^o$. The advance ratio was moderate ($\mu = 0.151$) and the rotor loading $C_T/\sigma = 0.057$ was moderate as well, compared to the rotor measurements given in Tab. 1. As in hover the tip vortices are strong on the retreating side since the local velocity is smaller, but the loading of the advancing side must be balanced by an equal loading on the retreating side. However, the loading gradient in the vicinity of the blade tip usually is weaker in forward flight.

Results for the data in the measurement plane

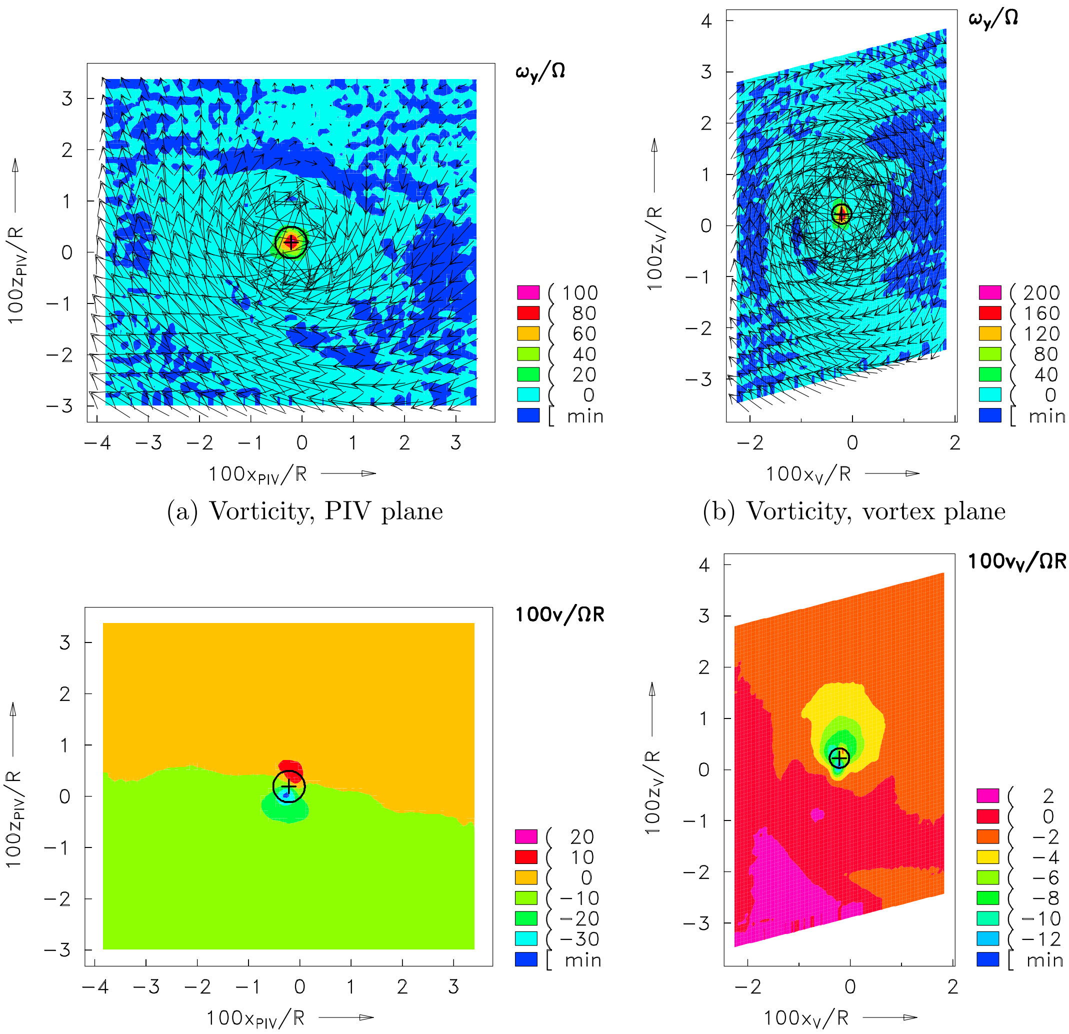

(a) Vorticity, PIV plane (b) Vorticity, vortex plane

(c) Cross-flow, PIV plane (d) Cross-flow, vortex plane

Figure 30: PIV data of the BL case (retreating side) in the measurement plane and rotated into the vortex axis system, pos. 52 of Fig. 1 (a), $\mu = 0.151$, $\psi_v = 34^o$.

Parameter	PIV	IA	CA	SA
$\beta_x/^o$	0.0	0.1	0.3	1.3
$\beta_z/^o$	0.0	-24.2	-24.9	-23.9
ω_0/Ω	114.3	123.8	135.9	68.7
$v_0/\Omega R$	0.264	0.252	0.183	0.90
r_c/c	0.060	0.054	0.054	0.078
$V_{s,max}/\Omega R$	0.232	0.246	0.244	0.173
n	1.2	1.2	1.2	1.1

Table 8: Rotation angles and tip vortex parameters in hover, $\psi_v = 44^o$. PIV: measurement plane, IA: average of individual, CA: conditional average, SA: simple average.

as well as after rotation into the vortex axis system are given in Fig. 30. A large rotation with $\beta_z = 55^o$ about the z-axis is identified, which is in agreement with the orientation of the predicted vortex axis and the PIV plane shown in Fig. 1. About the x-axis a rotation of $\beta_x = 10^o$ is found.

These rotation angles result in a strong compression of the x-axis, plus a significant shear of the measurement grid. As a consequence, the peak value of vorticity in the vortex axis system, Fig. 30 (b), is twice as large as in the measurement plane, (a), and the vector field appears more rotational symmetric. The cross-flow component in the measurement plane shown in (c) has large contributions from the swirl velocity at the core radius. In the vortex axis system, (d), only the axial velocity peak in the vortex center is left, and the entire area outside the core radius has about zero cross-flow.

In Tab. 9, the results of parameter identification are given together with the simple average results. At this age the vortex has a maximum swirl velocity of almost 23% of the tip speed and a core radius of little more than 3% chord, which are less than in hover. At this early stage of the

Parameter	PIV	CA	SA
$\beta_x/^o$	0.0	10.1	10.8
$\beta_z/^o$	0.0	55.6	52.1
ω_0/Ω	1.104	2.245	1.442
$v_0/\Omega R$	-0.326	-0.126	-0.096
r_c/c	0.051	0.032	0.042
$V_{s,max}/\Omega R$	0.172	0.225	0.193
n	1.0	1.1	1.1

Table 9: Rotation angles and tip vortex parameters on the retreating side, pos. 52 of Fig. 1, $\mu = 0.151$, $\psi_v = 34^o$. CA: conditional average, SA: simple average.

Parameter	PIV	CA	SA
$\beta_x/^o$	0.0	1.5	2.6
$\beta_z/^o$	0.0	-44.6	-45.0
ω_0/Ω	33.6	56.3	43.2
$v_0/\Omega R$	0.113	0.058	0.050
r_c/c	0.061	0.045	0.051
$V_{s,max}/\Omega R$	0.070	0.087	0.081
n	1.2	1.2	1.4

Table 10: Rotation angles and tip vortex parameters on the advancing side, pos. 29 of Fig. 1, $\mu = 0.151$, $\psi_v = 6^o$. CA: conditional average, SA: simple average.

vortex age the peak axial velocity in the vortex center is found to be almost 13% of the tip speed directed towards the generating blade. Again, this value is less than that for the hover case.

The rotation angles of the simple average agree well with those of the conditional average. As in the hover case, the vorticity peak, the maximum swirl velocity and the axial velocity peak in the vortex center are significantly reduced, and the core radius is identified much larger, compared to the conditional average.

4.3 BL case, advancing side

The measurement of pos. 29 of Fig. 1 is presented here, where the blade position was at $\psi = 110^o$ and the measurement location at $\psi = 104^o$, such that the vortex age is only $\psi_v = 6^o$ and the data were taken shortly behind the trailing edge of the generating blade. In this case the shear layer of the blade is visible in the distribution of vorticity in Fig. 31 (a) and of comparable strength of the tip vortex itself. The vector field appears elliptical as expected for an inclination of the vortex axis with respect to the measurement plane. After rotation into the vortex axis system, which required a rotation of $\beta_z = -45^o$ and $\beta_x = 2^o$ the vector field appears rotational symmetric and the peak value of vorticity in the vortex center is almost twice as large, (b).

The cross-flow distribution in the measurement plane, Fig. 31 (c), shows effects of vortex inclination at the core radius as in the hover case, plus the influence of the shear layer. Global gradients from top to bottom are present as well, but these disappear after rotation into the vortex system shown in (d). Here a peak cross-flow velocity is present in the vortex center, directed towards the vortex creating blade, and additionally the drag hump of the shear layer is well visible here. The area outside these structures now has zero cross-flow as expected. Note that the axial velocity peak value in the vortex center is of the same magnitude as the drag hump of the shear layer.

In Tab. 10, the results of parameter identification are given together with the results from the simple average. At this age the vortex has a maximum swirl velocity of only 9% of the tip speed, which is significantly less than in hover, and a core radius of little more than 4% chord, which is slightly less than in hover. At this early stage of the vortex age the peak axial velocity in the vortex center is found to be almost 6% of the tip speed and directed towards the generating blade. Again, this value is significantly less than that for the hover case.

As in hover and on the retreating side of the BL case, the rotation angles appear very similar in both conditional and simple average. Also, the vorticity peak, the maximum swirl velocity and the axial velocity peak in the vortex center are significantly reduced, and the core radius is identified much larger, compared to the conditional average.

4.4 Blade circulation and vortex circulation

The bound circulation of the lifting blade is related to the vortex circulation. Ideally the vortex strength equals the maximum circulation of the lifting blade, but in real world the vortex is created by a continuous distribution of vorticity with varying strength trailed into the wake along the span. This rolls up into a tip vortex within a short range behind the trailing edge. In hover, where the peak blade circulation is located close to the tip, the roll-up to a vortex is finished very early, but in cases where the circulation gradient towards the tip is low or close to zero the roll-up can take much more time, up to a complete rotor revolution.

In the cases investigated here, the hover vortex is well defined at its age of $\psi_v = 44^o$, and the same is true for the forward flight in the BL case on the retreating side, although some contribution of a shear layer is visible and indicates a

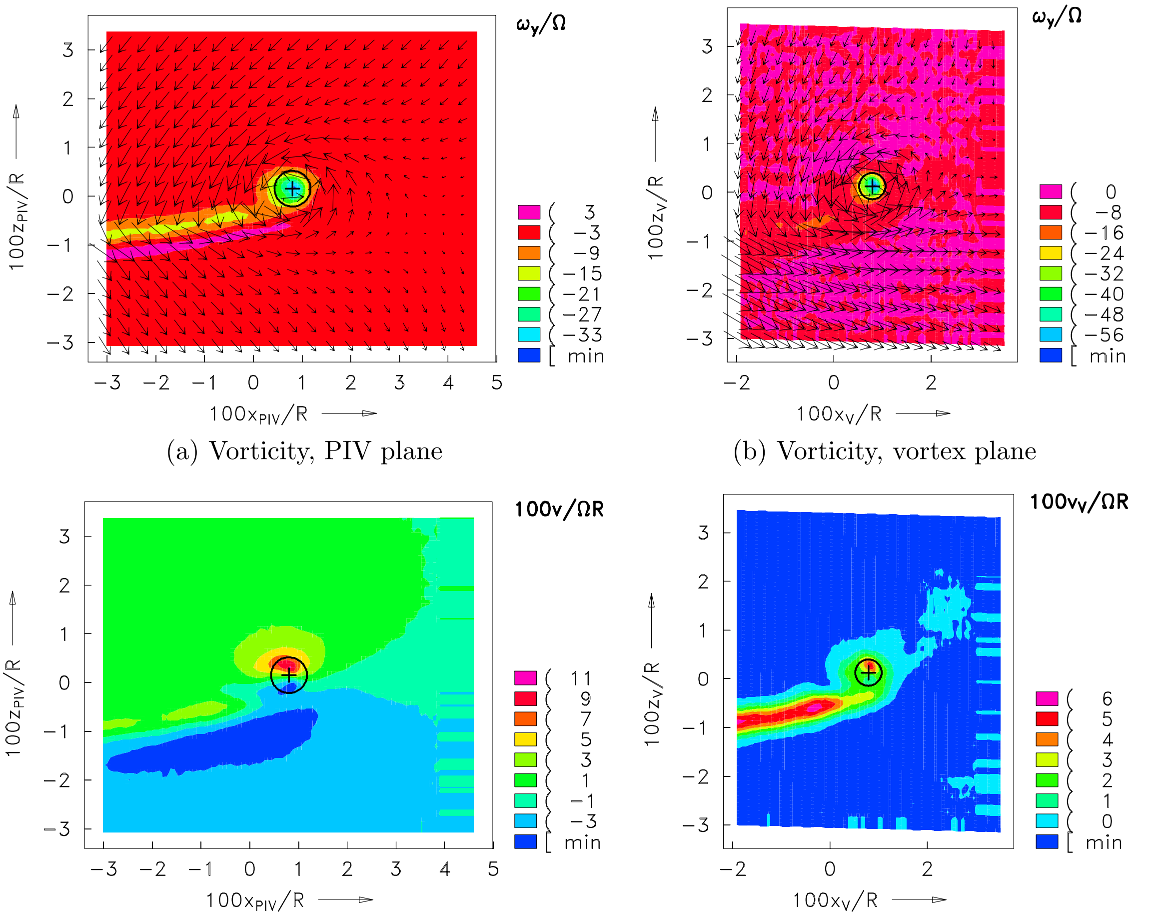

(a) Vorticity, PIV plane (b) Vorticity, vortex plane

(c) Cross-flow, PIV plane (d) Cross-flow, vortex plane

Figure 31: PIV data of the BL case (advancing side) in the measurement plane and rotated into the vortex axis system, pos. 29 of Fig. 1 (a), $\mu = 0.151$, $\psi_v = 6^o$.

weaker radial gradient of bound circulation. On the advancing side the shear layer is even stronger and its vorticity content is of the same order of magnitude as the vortex created right at the tip of the blade.

Since in HART II only the radial station of $r/R = 0.87$ was fully instrumented, no radial distribution of circulation can be extracted. The HART test of 1994 [30], however, had the same operational conditions as investigated here, but had fully instrumented sections at $r/R = 0.75$, 0.87 and 0.97. Assuming the lift and thus the circulation drops to zero at the blade tip itself, the radial distribution of circulation for hover and the BL case is shown in Fig. 32.

The values of the bound circulation at $r/R = 0.94$ are extracted from Fig. 32 and compared to the circulation at the core radius of the associated blade tip vortices, Γ_v, in Tab. 11. This vortex circulation is related to the maximum swirl and the n parameter by $\Gamma_v = 2^{1+1/n}\pi r_c V_{s,max}$ using a Vatistas vortex model, see App. A. The vortex parameters n, r_c and $V_{s,max}$ are taken from Tab. 8, Tab. 9 and Tab. 10. A large fraction of

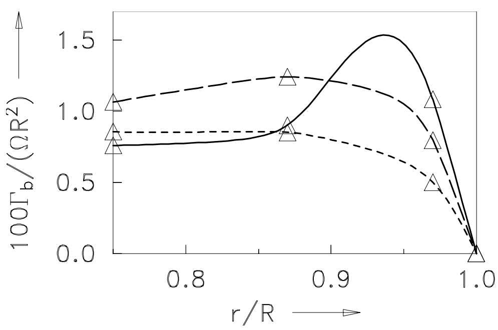

Figure 32: Radial distribution of blade bound circulation from the HART test of 1994. Solid: hover; dotted: BL, $\psi = 104^o$; dashed: BL, $\psi = 256^o$.

the bound circulation is contained in the tip vortex in the hover case, which is a consequence of the steep radial gradient of blade circulation. The maximum of the blade circulation in hover could only be guessed, in this case additional instrumented sections between $r/R = 0.87$ and 0.97 would be necessary.

The BL cases show the maximum of bound cir-

case	$\psi/^o$	$\frac{100\Gamma_b}{\Omega R^2}$	$\psi_v/^o$	$\frac{100\Gamma_v}{\Omega R^2}$	$\frac{\Gamma_v}{\Gamma_b}$
hover	136	1.535	44	0.914	0.60
BL	256	1.118	34	0.517	0.46
BL	104	0.686	6	0.257	0.37

Table 11: Blade circulation at $r/R = 0.94$ and circulation of the tip vortex at the core radius.

culation much more inboard, at $r/R = 0.87$ for the retreating side and between $0.8 < r/R < 0.87$ on the advancing side. Consequently the radial gradients are weaker and vorticity in the associated shear layers is visible in the PIV data, especially on the advancing side, see Fig. 31 (a). Therefore, the vortices contain only a smaller fraction of the blade bound circulation in their core, and the remaining part is distributed in the shear layer outside the vortex core. This part gets rolled up into the vortex at larger vortex ages [31].

5 Conclusions

3C-PIV vector field processing for proper analysis of vortex parameters requires several methodologies to be applied. Using numerically generated virtual PIV data these methods are validated.

1. Spurious vector elimination is needed, otherwise artificial vorticity is created by these that often is stronger than that of the flow field itself.

2. Various methodologies exist to compute velocity gradients, but care must be taken in application since some of them tend to increase noise artificially, and others tend to smooth the data too much. This depends on parameters of the pre-processing, like oversampling.

3. The identification of vortex centers is best performed using the area center of the distribution of a representative scalar value. This can be vorticity (but this has a bad signal-to-noise ratio), or flow field operators like λ_2 or Q that additionally suppress apparent vorticity of shear layers from the wake of the blade. Further improvements are obtained using a convolution of normalized functions representing the expected distribution with the scalar fields.

4. Conditional averaging is mandatory for analysis of vortex properties since it retains the peak values of individual characteristics and simultaneously eliminates noise. Due to vortex wander (and camera motion), the ensemble (or simple) average results in artificially large core radii and significantly lower swirl velocities. However, for the identification of the average location the ensemble average can be used.

5. The mean identification of the mean velocity is complicated by the presence of the vortex flow field, and by shear layers from the blades. The mean in-plane velocities can be analysed from the vortex center under the assumption that the vortex convects with the local mean flow. The mean out-of-plane or cross-flow velocity must be analysed from the flow outside the vortex proximity since the vortex itself has an axial velocity that is not part of the mean, and that has a maximum in the vicinity of the vortex center itself.

6. In most measurements the vortex axis is not normal to the measurement plane. When the inclination angles exceed about 10^o the measurement plane must be re-oriented into the vortex axis system. This can be performed in the post-processing by identification of the rotation angles from the cross-flow and swirl velocities.

7. The vortex characteristics like core radius, maximum swirl and shape of the swirl profile can only be analysed in the vortex axis system, using some of the usual mathematical models.

The methodologies developed can be successfully applied to real world data like those obtained in the HART II test. Future work will put together the results for the creation of generalized vortex models to be used in rotor simulation environments, like prescribed or free-wake codes, for noise, vibration and performance prediction of rotors.

References

[1] J.T. Heineck, G.K. Yamauchi, A.J. Woodcock, L. Laurenco, *Application of Three-Component PIV to a Hovering Rotor Wake,* 56^{th} Annual Forum of the American Helicopter Society, Virginia Beach, VA, USA, 2000

[2] P.B. Martin, J.G. Pugliese, J.G. Leishman, S.L. Anderson, *Stereo PIV Measurements in the Wake of a Hovering Rotor,* 56^{th} Annual Forum of the American Helicopter Society, Virginia Beach, VA, USA, 2000

[3] G.K. Yamauchi, C.L. Burley, E. Mercker, K. Pengel, R. JanakiRam, *Flow Measurements of an Isolated Model Tilt Rotor,* 55^{th}

Annual Forum of the American Helicopter Society, Montreal, Canada, 1999

[4] M. Raffel, U. Seelhorst, C. Willert, *Vortical Flow Structures at a Helicopter Rotor Model Measured by LDV and PIV,* The Aeronautical Journal of the Royal Aeronautical Society, Vol. 102, No. 1012, pp. 221-227, 1998

[5] W.R. Splettstößer, B.G. van der Wall, B. Junker, K.-J. Schultz, P. Beaumier, Y. Delrieux, P. Leconte, P. Crozier, *The ERATO Programme: Wind Tunnel Results and Proof of Design for an Aeroacoustically Optimized Rotor,* 25^{th} European Rotorcraft Forum, Rome, Italy, 1999

[6] H. Richard, M. Raffel, *Rotor Wake Measurements: Full-scale and Model Tests,* 58^{th} Annual Forum of the American Helicopter Society, Montreal, Canada, 2002

[7] H. Kato, S. Watanabe, N. Kondo, S. Saito, *Application of Stereoscopic PIV to Helicopter Rotor Blade Tip Vortices,* 20^{th} Congress on Instrumentation in Aerospace Simulation Facilities, Göttingen, Germany, 2003

[8] A. Murashige, N. Kobiki, A. Tsuchihashi, H. Nakamura, K. Inagaki, E. Yamakawa, *ATIC Aeroacoustic Model Rotor Test at DNW,* 24^{th} European Rotorcraft Forum, Marseilles, France, 1998

[9] A. Murashige, N. Kobiki, A. Tsuchihashi, K. Inagaki, T. Tsujiutchi, Y. Hasegawa, H. Nakamura, Y. Yamamoto, E. Yamakawa, *Second ATIC Aeroacoustic Model Rotor Test at DNW,* 26^{th} European Rotorcraft Forum, The Hague, Netherlands, 2000

[10] K.W. McAlister, *Rotor Wake Development During the First Revolution,* Journal of the American Helicopter Society, Vol. 49, No. 4, 2004

[11] Y. Yu, *The HART II Test - Rotor Wakes and Aeroacoustics with Higher-Harmonic Pitch Control (HHC) Inputs - The Joint German/French/Dutch/US Project -,* 58^{th} Annual Forum of the American Helicopter Society, Montreal, Canada, 2002

[12] B.G. van der Wall, B. Junker, Y.H. Yu, C.L. Burley, T.F. Brooks, C. Tung, M. Raffel, H. Richard, W. Wagner, E. Mercker, K. Pengel, H. Holthusen, P. Beaumier, Y. Delrieux, *The HART II Test in the LLF of the DNW - a Major Step towards Rotor Wake Understanding,* 28^{th} European Rotorcraft Forum, Bristol, England, 2002

[13] M. Raffel, H. Richard, K. Ehrenfried, B.G. van der Wall, C.L. Burley, P. Beaumier, K. McAlister, K. Pengel, *Recording and Evaluation Methods of PIV Investigations on a Helicopter Rotor Model,* Experiments in Fluids, Vol. 36, No. 1, pp. 146-156, 2004

[14] M. Raffel, C. Willert, J. Kompenhans, *Particle Image Velocimetry, A Practical Guide,* Springer, ISBN 3-540-63683-8, 1998

[15] C.L. Burley, T.F. Brooks, B.G. van der Wall, H. Richard, M. Raffel, P. Beaumier, Y. Delrieux, J.W. Lim, Y.H. Yu, C. Tung, K. Pengel, E. Mercker, *Rotor Wake Vortex Definiton and Validation from 3-C PIV HART II Study,* 28^{th} European Rotorcraft Forum, Bristol, England, 2002

[16] J. Bailly, Y. Delrieux, P. Beaumier, *VHART II: Experimental Analysis and Validation of ONERA Methodology for the Prediction of Blade-Vortex Interaction,* 30^{th} European Rotorcraft Forum, Marseille, France, 2004

[17] B.G. van der Wall, *Vortex Characteristics Analysed from HART Data,* 23^{rd} European Rotorcraft Forum, Dresden, Germany, 1997

[18] G.H. Vatistas, V. Kozel, *A simpler model for concentrated vortices,* Experiments in Fluids, Vol. 11, pp. 73-76, 1991

[19] F. Scarano, *Iterative Image Deformation Methods in PIV,* Measurement Science and Technology, Vol. 13, pp. R1-R19, 2002

[20] M. Stanislas, K. Okamoto, C.J. Kähler, J. Westerweel, *Main Results of the Second International PIV Challenge,* Experiments in Fluids, Vol. 38, pp. 1432-1114, 2005

[21] J. Jeong, F. Hussain, *On the Identification of a Vortex,* Journal of Fluid Mechanics, Vol. 285, pp. 69-94, 1995

[22] J. Hunt, A. Wray, P. Moin, *Eddies, Stream and Convergence Zone in Turbulent Flows,* CTR-S88, Stanford Center for Turbulence Research, p. 193, 1988

[23] H.J. Lugt, *Introduction to Vortex theory,* ISBN 0-9657689-0-2, Vortex Flow Press, Potomac, Maryland, 1996

[24] J. Ebling, G. Scheuermann, B.G. van der Wall, *Analysis and Visualization of 3C-PIV Images from HART II using Image Processing Methods,* EUROGRAPHICS-IEEE VGTC Symposium on Visualization, Leeds, England, 2005

[25] C.W. Oseen, *Über Wirbelbewegung in einer reibenden Flüssigkeit,* Ark. Mat. Astron. Fys., Vol. 7, No. 14, pp. 14-21, 1911

[26] H. Lamb, *Hydrodynamics,* Cambridge University Press, Cambridge, UK, pp. 592-593, 668-669, 1932

[27] B.G. Newman, *Flow in a Viscous Trailing Vortex,* Aeronautical Quarterly, May, pp. 167-188, 1959

[28] G. Hamel, *Spiralförmige Bewegungen zäher Flüssigkeiten,* J.-Ber. Deutsch. Math.-Verein, Vol. 25, p. 34, 1917

[29] P.B. Martin, J.G. Leishman, *Trailing Vortex Measurements in the Wake of a Hovering Rotor Blade with Various Tip Shapes,* 58^{th} Annual Forum of the American Helicopter Society, Montreal, Canada, 2002

[30] W.R. Splettstößer, R. Kube, U. Seelhorst, W. Wagner, A. Boutier, F. Micheli, E. Mercker, K. Pengel, *Key Results from a Higher Harmonic Control Aeroacoustic Rotor Test (HART) in the German-Dutch Wind Tunnel,* 21^{st} European Rotorcraft Forum, Saint-Petersburg, Russia, 1995

[31] B.G. van der Wall, C.L. Burley, Y.H. Yu, H. Richard, K. Pengel, P. Beaumier, *The HART II test - measurement of helicopter rotor wakes,* Aerospace Science and Technology, Vol. 8, pp. 273-284, 2004

A The relation between swirl and flow field operators

A.1 Dimensions

All variables are made non-dimensional, i.e. the velocities are divided by ΩR, circulation and kinematic viscosity by ΩR^2, vorticity by Ω, coordinates by the core radius r_c, the core radius by R and the flow field operators by Ω^2.

A.2 Vatistas model of swirl

Vatistas model describes the swirl velocity in terms of the radial distance to the vortex center r and a shape parameter n that represents the "sharpness" of the maximum swirl velocity peak and thus the distribution of vorticity [18].

$$\begin{aligned} r &= \sqrt{x^2+z^2} \\ V_s &= V_{s0}\frac{r}{(1+r^{2n})^{1/n}} \\ u &= -V_s\frac{z}{r} \\ w &= V_s\frac{x}{r} \end{aligned}$$

In this case, $V_{s0} = \Gamma_v/(2\pi r_c) = V_{s,max}2^{1/n}$ since at the core radius $r = 1$ and hence $V_s = V_{s0}/2^{1/n}$. The flow derivatives with respect to the coordinate directions x and z can analytically be derived. When simplifying for $z = 0$ since the flow field is rotationally symmetric,

$$\begin{aligned} \left.\frac{\partial u}{\partial z}\right|_{z=0} &= -\frac{V_{s0}}{(1+x^{2n})^{1/n}} \\ \left.\frac{\partial w}{\partial x}\right|_{z=0} &= -V_{s0}\frac{x^{2n}-1}{(1+x^{2n})^{1/n+1}} \\ \left.\frac{\partial u}{\partial x}\right|_{z=0} &= \left.\frac{\partial w}{\partial z}\right|_{z=0} = 0 \end{aligned}$$

Then, the vorticity and λ_2 parameter are (the result for Q is identical to that for λ_2)

$$\begin{aligned} \omega|_{z=0} &= \left(\frac{\partial u}{\partial z}-\frac{\partial w}{\partial x}\right)/2 \\ &= -\frac{V_{s0}}{(1+x^{2n})^{1/n+1}} \\ \lambda_2|_{z=0} &= \left(\frac{\partial u}{\partial x}^2+\frac{\partial w}{\partial z}^2\right)/2+\frac{\partial w}{\partial x}\frac{\partial u}{\partial z} \\ &= -V_{s0}^2\frac{1-x^{2n}}{(1+x^{2n})^{2/n+1}} \\ Q|_{z=0} &= \frac{\left(\frac{\partial u}{\partial x}+\frac{\partial w}{\partial z}\right)^2}{4}-\frac{\partial u}{\partial x}\frac{\partial w}{\partial z}+\frac{\partial w}{\partial x}\frac{\partial u}{\partial z} \\ &= \lambda_2|_{z=0} \end{aligned}$$

In the vortex center, i.e. at $r = x = z = 0$, they become

$$\begin{aligned} \omega|_{r=0} &= -V_{s0} = -V_{s,max}2^{1/n} \\ \lambda_2|_{r=0} &= -V_{s0}^2 = -\left(\omega|_{r=0}\right)^2 \end{aligned}$$

Since the flow operators are constant in the vortex center their radial gradients are zero there. Although these operators often appear to have a sharp spike there is no discontinuity and thus the sharp spike is just an effect of scarseness of the grid. A significant higher grid density would result in a well rounded maximum of these operators in the vortex center. At the core radius, i.e. at $x = 1$,

$$\begin{aligned} \omega|_{z=0,x=1} &= -\frac{V_{s0}}{2^{1/n+1}} = -\frac{V_{s,max}}{2} \\ \lambda_2|_{z=0,x=1} &= 0 \end{aligned}$$

At the vortex center the vorticity represents the negative gradient $-\partial V_s/\partial r$. For the Vatistas model,

$$\omega|_{r=0} = -\frac{\partial V_s}{\partial r} = -V_{s0}\frac{1-r^{2n}}{(1+r^{2n})^{1/n+1}}$$

For $r = 0$ this results in $\omega|_{r=0} = -V_{s0}$ as is written above. At the core radius, i.e. $r = 1$, the vorticity is expressed by half of the maximum swirl velocity, $\omega|_{r=1} = -V_{s,max}/2$.

A.3 Lamb-Oseen and Newman vortex

This description of a vortex is an analytical solution of the Navier-Stokes equation [25, 26, 28]. Newman added an axial flow component [27]. Its swirl velocity field is described by

$$V_s = V_{s0}\frac{1-e^{-\alpha r^2}}{r}$$

with V_{s0} as before and where $\alpha = 1/(4\nu\psi_v)$ represents the time decay with ν as the kinematic viscosity. At the time of vortex creation, $\psi_v = 0$, the potential vortex is obtained with zero core radius and infinite swirl at the center. As $\psi_v \to \infty$ the vortex disappears. For a given age this can be set to a constant value of $\alpha = 1.25643$ [26] and the result for the flow derivatives at $z = 0$ is

$$\left.\frac{\partial u}{\partial z}\right|_{z=0} = -V_{s0}\frac{1-e^{-\alpha x^2}}{x^2}$$
$$\left.\frac{\partial w}{\partial x}\right|_{z=0} = -V_{s0}\frac{1-e^{-\alpha x^2}-2\alpha x^2 e^{-\alpha x^2}}{x^2}$$

The other derivatives are zero. Then, the flow field operators are

$$\omega|_{z=0} = -V_{s0}\alpha e^{-\alpha x^2}$$
$$\lambda_2|_{z=0} = -V_{s0}^2\left(e^{-\alpha x^2}-1\right)\frac{1-e^{-\alpha x^2}-2\alpha x^2 e^{-\alpha x^2}}{x^4}$$

In the vortex center, where $r = x = z = 0$, the result for λ_2 is obtained using Bernoulli l' hospital rule until a finite value is reached.

$$\omega|_{r=0} = -V_{s0}\alpha = -V_{s,max}\frac{\alpha}{1-e^{-\alpha}}$$
$$\lambda_2|_{r=0} = -V_{s0}^2\alpha^2 = -\left(\omega|_{r=0}\right)^2$$

In agreement with the section before the radial gradients of the flow operators at the vortex center are zero. At the core radius, where $x = 1$,

$$\omega|_{z=0,x=1} = -V_{s0}\alpha e^{-\alpha}$$
$$\lambda_2|_{z=0,x=1} = 0$$

Here the maximum swirl velocity is present.

$$V_{s,max} = V_{s0}\left(1-e^{-\alpha}\right)$$

A.4 Circulation

The total circulation Γ_∞ of a potential vortex is given by the product of swirl velocity and the radius. This product is constant at any radius such that $\Gamma_\infty = 2\pi V_s r$ since all the vorticity is confined at an infinitesimal point in the vortex center. In contrast, the Vatistas and Lamb-Oseen model have a radial distribution of vorticity with a finite maximum in the vortex center and asymptotically approaching zero at large radii. Therefore, the circulation grows from the vortex center and asymptotically reaches its final value for large radii. For any value of n the Vatistas and Lamb-Oseen vortex models asymptotically approach the potential vortex result for large radii r. The total circulation of a Vatistas type of vortex is thus (note that $V_{s0} = \Gamma_v/(2\pi r_c)$

$$\Gamma_\infty = 2\pi r V_s|_{r\to\infty}$$
$$= 2\pi V_{s0} = \frac{\Gamma_v}{r_c} = 2\pi V_{s,max}2^{1/n}$$

and the circulation profile, i.e. the development of circulation, starting from the center of the vortex, is found by area integration of the vorticty

$$\Gamma = 2\int_0^{2\pi}\int_0^r \omega\, r\, dr\, d\phi$$
$$= -2\pi V_{s0}\frac{r^2}{(1+r^{2n})^{1/n}}$$
$$\frac{|\Gamma|}{\Gamma_\infty} = \frac{r^2}{(1+r^{2n})^{1/n}}$$

In the vortex center, where $r = 0$, the circulation is zero, and for large radii the ratio reaches the value of one. At the core radius, where $r = 1$,

$$|\Gamma|_{r=1} = \frac{\Gamma_\infty}{2^{1/n}} = \frac{\Gamma_v}{2^{1/n}r_c} = 2\pi V_{s,max}$$

For $n = 1$, which is known as the Scully vortex, half of the total circulation is contained within the core radius. As $n \to \infty$, which represents the Rankine vortex, all of the vorticity and hence the circulation is within the core radius, and nothing left outside (outside the core radius the flow field of a potential vortex is present). A lot of measurements fit to a value of $n = 2$ such that 70.7% of the total circulation is within the core.

For the Lamb-Oseen vortex the total circulation is easily derived for large radii and the circulation profile is then

$$\begin{aligned}
\Gamma_\infty &= 2\pi V_s r|_{r\to\infty} = 2\pi V_{s0} = 2\pi \frac{V_{s,max}}{1-e^{-\alpha}} \\
\frac{|\Gamma|}{\Gamma_\infty} &= 1 - e^{-\alpha r^2}
\end{aligned}$$

At the vortex core this type of vortex has 71.5% of its total circulation, which is close to the Vatistas vortex using a value of $n = 2$.